DALHOUSIE UNIVERSITY

Experimental study of reaction textures in volcaniclastic kimberlites

Kanwar Multani

SUBMITTED IN PARTIAL FULFILLMENT OF THE REQUIREMENTS FOR
THE DEGREE OF BACHELOR OF SCIENCES, HONOURS
DEPARTMENT OF EARTH SCIENCES
DALHOUSIE UNIVERSITY, HALIFAX, NOVA SCOTIA

April 2019

Distribution License

DalSpace requires agreement to this non-exclusive distribution license before your item can appear on DalSpace.

NON-EXCLUSIVE DISTRIBUTION LICENSE

You (the author(s) or copyright owner) grant to Dalhousie University the non-exclusive right to reproduce and distribute your submission worldwide in any medium.

You agree that Dalhousie University may, without changing the content, reformat the submission for the purpose of preservation.

You also agree that Dalhousie University may keep more than one copy of this submission for purposes of security, back-up and preservation.

You agree that the submission is your original work, and that you have the right to grant the rights contained in this license. You also agree that your submission does not, to the best of your knowledge, infringe upon anyone's copyright.

If the submission contains material for which you do not hold copyright, you agree that you have obtained the unrestricted permission of the copyright owner to grant Dalhousie University the rights required by this license, and that such third-party owned material is clearly identified and acknowledged within the text or content of the submission.

If the submission is based upon work that has been sponsored or supported by an agency or organization other than Dalhousie University, you assert that you have fulfilled any right of review or other obligations required by such contract or agreement.

Dalhousie University will clearly identify your name(s) as the author(s) or owner(s) of the submission, and will not make any alteration to the content of the files that you have submitted.

If you have questions regarding this license please contact the repository manager at dalspace@dal.ca.

Grant the distribution license by signing and dating below.

_____ _____

Name of signatory Date

TABLE OF CONTENTS

LIST OF FIGURES

LIST OF TABLES

ABSTRACT

Some of the most famous diamond deposits are associated with Kimberly-type pyroclastic kimberlite facies (KPK) located within diatreme part of kimberlite pipes. The origin of this type of kimberlite is one of the most debatable topics in kimberlite geology. The two competing models suggest either 1) explosive pyroclastic eruption with subsequent welding of the pyroclasts or 2) in-situ magma fragmentation without the formation of a pyroclastic deposit. The latter model suggests that a reaction between silicate fragments of the country rock and carbonatitic magma exsolves CO_2 causing the magma fragmentation and freezing. Furthermore, an extensive interaction between carbonate-rich kimberlite magma and silicate country rocks was recently proposed for Snap Lake kimberlite dyke. This experimental study tested the two hypotheses by examining the reaction of felsic, intermediate, and mafic xenoliths with four carbonate-rich kimberlite mixtures (AN-1 and LS-26) and carbonate compositions. The experiments are conducted in a box furnace and in a piston-cylinder apparatus at Dalhousie University at 800-1100°C and pressure of 0.1 MPa and ~500 MPa to explore the effect of temperature, CO_2, and H_2O on the textures and the sequence of the reaction minerals.

Experimental results show greater degree of reaction and assimilation of xenoliths in the absence of H_2O than in H_2O-bearing runs. Experiments conducted at 0.1 MPa showed greater degree of assimilation with the mafic and felsic xenoliths and the carbonate-rich mixture. In $CaCO_3$-Na_2CO_3 mixture runs, excessive CO_2 degassing ruptured the capsule due to over-pressure. H_2O bearing runs showed minimal to no reactions of the intermediate and mafic rocks with the kimberlite mixture. Additionally, Mg-rich LS-26 runs showed formation of Mg- and Fe-oxides encompassed by impure carbonate matrix. The developed reaction mineral phases and their textures were compared to the textures of natural BK1 Orapa KPKs of Botswana, Snap Lake, and Gahcho Kue kimberlites. Diffusion and dissolution of CaO and Na_2O components reflected in compositional gradients experienced by the xenoliths during experimental metasomatism. Perovskite was the most common and stable phase that crystallized in all runs conducted with AN-1 mixture. H_2O appears to have repressed the degree to which CO_2 would exsolve and react with the xenoliths.

Keywords: Kimberly-type pyroclastic kimberlites, diatreme zone, magmaclast, subvolcanic-fluidization model, metasomatism, perovskite, piston cylinder, diamonds.

LIST OF ABBREVIATIONS

AN	Anaconda Kimberlite Dyke
LS	Leslie Kimberlite Dyke
CK	Coherent Kimberlite
HK	Hypabyssal Kimberlite
FALC	Fort à la Corne Kimberlite
FPK	Fragmented Pyroclastic Kimberlite
KPK	Kimberley-Type Pyroclastic Kimberlite
VK	Volcaniclastic Kimberlite
Carb	Carbonate
REEs	Rare Earth Elements
C.I.	Contamination Index
EDS	Energy-Dispersive Spectroscopy
SEM	Scanning Electron Microscope

ACKNOWLEDGEMENTS

I would like to thank Dr. Yana Fedortchouk for providing me with the opportunity to conduct research on the wonderful world of kimberlites. She always had time to answer my questions and helped me get to know the ins and outs of experimental petrology. She continuously reminded me to stay on topic with my research when my writing derailed and spent countless hours providing me with constructive feedback throughout the writing stage to help me become a better writer. Although I still struggle.

I would like to thank Xiang and Dan for all their help with the EDS analysis. I would also like to thank the Department of Earth Sciences and all the professors in the department for providing a great learning environment and fun memories that I will cherish forever.

Lastly, this entire experience would have not been possible without the continuous encouragement and support of my family and friends who cheered me on to finish strongly.

CHAPTER 1 – INTRODUCTION

1.1 Overview of kimberlite occurrences and geology

Kimberlites are defined as low viscosity, volatile-rich (dominantly CO_2), potassic ultrabasic rocks that originate from deep-seated magmas in the mantle (Wooley et al., 1995). Kimberlites are a product of continental intra-plate magmatism and are mostly concentrated within ancient cratons, where they generally occur in clusters of similar age/source and the clusters can cover several hundred to thousands of square kilometres (Mitchell, 1986, Sparks, 2006). Kimberlite magma formation is associated with deeper plumes and/or metasomatic processes, whereas reactivation of major zones of weakness in the lithosphere, such as shallow fault zones and lineaments, controls the local emplacement of the kimberlites (Mitchell, 1986; Winter, 2010).

Kimberlites are different from other magmatic rocks in that they commonly exhibit a distinctive inequigranular texture resulting from the presence of macrocrysts (0.5-10mm diameter crystals), megacrysts (1-20 cm diameter crystals) set in fine-grained matrix with addition of xenoliths (Wooley et. al., 1995). Large amounts of mantle-derived material, significant alteration, and loss of volatiles and fine particles during explosive eruption, complicates the derivation of the composition of the primary kimberlite melt.

Kimberlites are one of the most common source-rock for diamonds, and have been discovered on all continents and the ages vary from Proterozoic to early Tertiary (Sparks, 2006). In Canada, over 30 comagmatic kimberlite fields have been discovered in Slave and Superior Archean cratons, Buffalo and Sask cratons, Rae, Hearne, and Arctic craton (Scott Smith, 2008). They are a product of partial melting of metasomatized, potassium-rich mantle sources, such as garnet harzburgites and/or carbonated lherzolite, and tend to originate at depths of 150 km or more (Mitchell, 1986; Winter, 2010). Kimberlites can occur as hypabyssal dikes or sills, diatremes, and crater-fill, each associated with a unique style of magmatic activity (Mitchell, 1986).

1.2 Kimberlite terminology and classification

Most of the earlier kimberlite terminology is based on the investigation of diamond mines in South Africa. More recent kimberlite pipe discoveries in Canada and their notable variability required a new classification approach to describe kimberlites and their related rocks in a practical and systematic manner. A new terminology and nomenclature were developed as a result of a team effort and is used in this study (Scott Smith et al., 2018). Figure 1.1 shows a systematic approach to kimberlite classification, where interpretation of the origin and the emplacement mechanism based on textural observations is presented in column “stage 3a and 3b”.

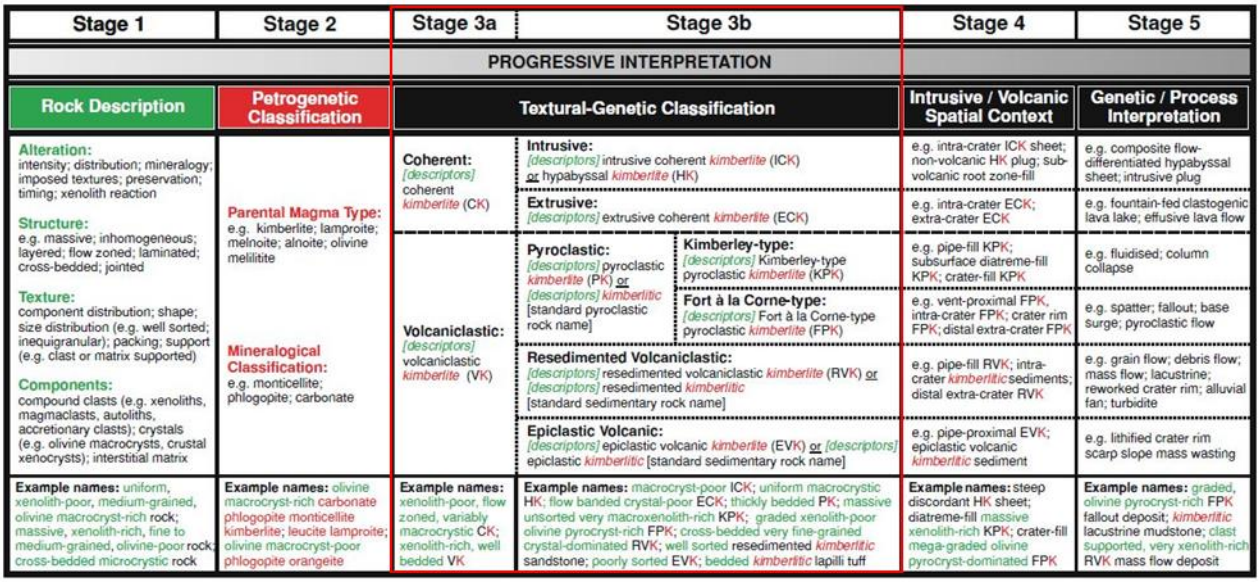

Stage 1	Stage 2	Stage 3a	Stage 3b		Stage 4	Stage 5
PROGRESSIVE INTERPRETATION						
Rock Description	**Petrogenetic Classification**	**Textural-Genetic Classification**			**Intrusive / Volcanic Spatial Context**	**Genetic / Process Interpretation**
Alteration: intensity; distribution; mineralogy; imposed textures; preservation; timing; xenolith reaction **Structure:** e.g. massive; inhomogeneous; layered; flow zoned; laminated; cross-bedded; jointed **Texture:** component distribution; shape; size distribution (e.g. well sorted; inequigranular); packing; support (e.g. clast or matrix supported) **Components:** compound clasts (e.g. xenoliths, magmaclasts, autoliths, accretionary clasts); crystals (e.g. olivine macrocrysts, crustal xenocrysts); interstitial matrix	**Parental Magma Type:** e.g. kimberlite; lamproite; melnoite; alnoite; olivine melilitite **Mineralogical Classification:** e.g. monticellite; phlogopite; carbonate	**Coherent:** *[descriptors]* coherent *kimberlite* (CK)	**Intrusive:** *[descriptors]* intrusive coherent *kimberlite* (ICK) or hypabyssal *kimberlite* (HK)		e.g. intra-crater ICK sheet; non-volcanic HK plug; sub-volcanic root zone-fill	e.g. composite flow-differentiated hypabyssal sheet; intrusive plug
			Extrusive: *[descriptors]* extrusive coherent *kimberlite* (ECK)		e.g. intra-crater ECK; extra-crater ECK	e.g. fountain-fed clastogenic lava lake; effusive lava flow
		Volcaniclastic: *[descriptors]* volcaniclastic *kimberlite* (VK)	**Pyroclastic:** *[descriptors]* pyroclastic *kimberlite* (PK) or *[descriptors] kimberlitic* [standard pyroclastic rock name]	**Kimberley-type:** *[descriptors]* Kimberley-type pyroclastic *kimberlite* (KPK)	e.g. pipe-fill KPK; subsurface diatreme-fill KPK; crater-fill KPK	e.g. fluidised; column collapse
				Fort à la Corne-type: *[descriptors]* Fort à la Corne-type pyroclastic *kimberlite* (FPK)	e.g. vent-proximal FPK, intra-crater FPK; crater rim FPK; distal extra-crater FPK	e.g. spatter; fallout; base surge; pyroclastic flow
			Resedimented Volcaniclastic: *[descriptors]* resedimented volcaniclastic *kimberlite* (RVK) or *[descriptors]* resedimented *kimberlitic* [standard sedimentary rock name]		e.g. pipe-fill RVK; intra-crater *kimberlitic* sediments; distal extra-crater RVK	e.g. grain flow; debris flow; mass flow; lacustrine; reworked crater rim; alluvial fan; turbidite
			Epiclastic Volcanic: *[descriptors]* epiclastic volcanic *kimberlite* (EVK) or *[descriptors]* epiclastic *kimberlitic* [standard sedimentary rock name]		e.g. pipe-proximal EVK; epiclastic volcanic *kimberlitic* sediment	e.g. lithified crater rim scarp slope mass wasting
Example names: uniform, xenolith-poor, medium-grained, olivine macrocryst-rich rock; massive, xenolith-rich, fine to medium-grained, olivine-poor rock; cross-bedded microcrystic rock	**Example names:** olivine macrocryst-rich carbonate phlogopite monticellite kimberlite; leucite lamproite; olivine macrocryst-poor phlogopite orangeite	**Example names:** xenolith-poor, flow zoned, variably macrocrystic CK; xenolith-rich, well bedded VK	**Example names:** macrocryst-poor ICK; uniform macrocrystic HK; flow banded crystal-poor ECK; thickly bedded PK; massive unsorted very macroxenolith-rich KPK; graded xenolith-poor olivine pyrocryst-rich FPK; cross-bedded very fine-grained crystal-dominated RVK; well sorted resedimented *kimberlitic* sandstone; poorly sorted EVK; bedded *kimberlitic* lapilli tuff		**Example names:** steep discordant HK sheet; diatreme-fill massive xenolith-rich KPK; crater-fill mega-graded olivine pyrocryst-dominated FPK	**Example names:** graded, olivine pyrocryst-rich FPK fallout deposit; *kimberlitic* lacustrine mudstone; clast supported, very xenolith-rich RVK mass flow deposit

Figure 1.1: Nomenclature scheme and systematic framework for the description, classification, and interpretation of kimberlites and related rocks. From Scott Smith et al. (2013).

Stage 3a distinguishes between coherent kimberlite (CK) and volcaniclastic kimberlites (VK) based on textural and mineralogical features (Scott Smith et al., 2018). A coherent kimberlite texture forms entirely from cooling and direct crystallization of magma or lava without any notable fragmentation where pre-existing crystals are set in an interstitial matrix that is composed of quenched or crystalline groundmass formed from crystallization of the kimberlite melt (Figure 1.2a, Scott Smith et al., 2018). Volcaniclastic kimberlite comprises of a substantial proportion of volcanic particles that can be of any shape or size and does not pertain to any specific clast-forming process (Scott Smith et al., 2018).

Stage 3b further subdivides the coherent kimberlites into intrusive (hypabyssal kimberlites) and extrusive CK (lavas). This requires further descriptors based on spatial and contact relationships (Scott Smith et al., 2018). Volcaniclastic kimberlites are further subdivided into (i) pyroclastic kimberlites (PK), (ii) resedimented volcaniclastic kimberlites (RVK) and (iii) epiclastic kimberlites (EK). Pyroclastic kimberlites are a product of explosive volcanic eruption and are deposited or emplaced by pyroclastic processes and demonstrate no evidence for resedimentation (Scott Smith et al., 2018). RVKs form by sedimentary re-deposition of unconsolidated pyroclastic and other surficial material (Scott Smith et al., 2018). Primary movement of material towards the vent is required in order to form pipe-fill RVK (Scott Smith et al., 2018). EKs are formed by surface processes (erosion, transportation, and deposition) and consist of detritus containing epiclasts derived from exposed lithified volcanic kimberlites (Scott Smith et al., 2018).

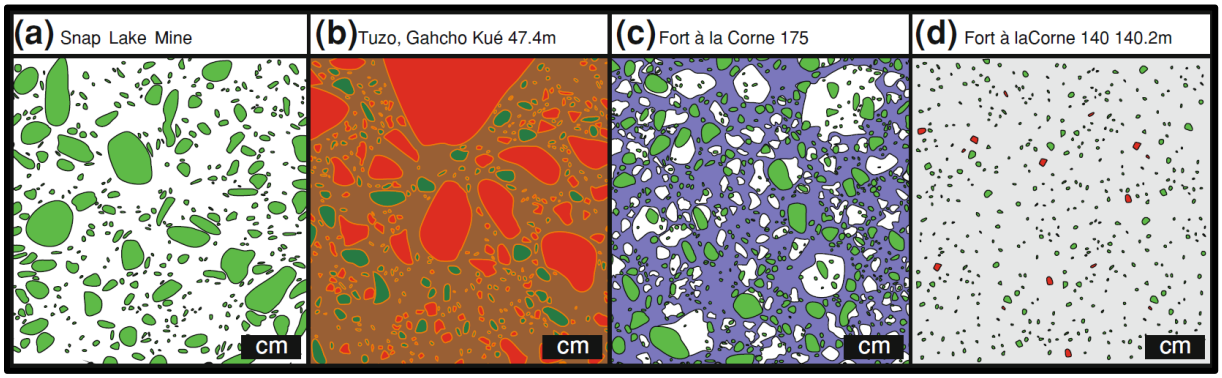

Figure 1.2: Kimberlite textures from various kimberlite mines across Canada at varying depths. (a) Sheet infilled HK from the Snap Lake Mine, NWT showing macrocrystic olivines (green) in fine grained matrix. (b) Diatreme filled KPK from the Gahcho Kue Diamond Mine Complex, NWT showing varying sizes of country rock xenoliths (red) with pseudomorphed olivines (green) surrounded by interclast matrix (brown). (c) Crater-Fill macrocrystic FPK from the Fort a la Corne mine, SK showing non-discrete and discrete melt-bearing (white) olivine pyroclasts (green) surrounded by interclast matrix. (d) Crater-Fill microcrystic FPK fill with gradations showing country rock xenoliths (red) and olivines (green) in very-fine grained matrix. From Scott Smith et al. (2018).

Pyroclastic kimberlites are further sub-divided into two classes: (i) Kimberley-type pyroclastic kimberlite (KPK), and (ii) Fort a la Corne-type pyroclastic kimberlite (FPK). KPKs are distinct from FPKs in that the components, such as xenoliths, olivine macrocrysts, and magmaclasts are set in a fine-grained interclast matrix with a

distinctive microlitic component that is unique to KPK and are described in more detail in *Section 1.4*. KPKs are the dominant infill of the diatreme zones (see *Section 1.3*) in some kimberlite pipes around the world and are economically important due to discoveries of diamonds within the diatreme zone (Scott Smith et al., 2018). FPKs are clast supported with graded bedding that contain melt bearing pyroclasts, fresh to totally pseudomorphed olivines, and cryptocrystalline groundmass representing rapidly cooled-to-quenched melt (Figure 1.2c, d; Scott Smith et al., 2018). Melt bearing pyroclasts of FPK are often amoeboid to sub-spherical in shape with fluidal outlines and consists of olivine kernels in a rapidly cooled-to-quenched groundmass (Figure 1.3b; Mitchell et al., 2008). Separation of discrete grains of olivine are a characteristic feature of FPKs (Figure 1.3b). The melt-bearing pyroclasts (former pelletal lapilli or magmaclast) present in KPKs are typically sub-spherical in shape and are composed of single or multiple pseudomorphed kernels of olivine with minor melt selvage and the groundmass of the pyroclasts is indicative of coherent kimberlites (Scott Smith et al., 2018).

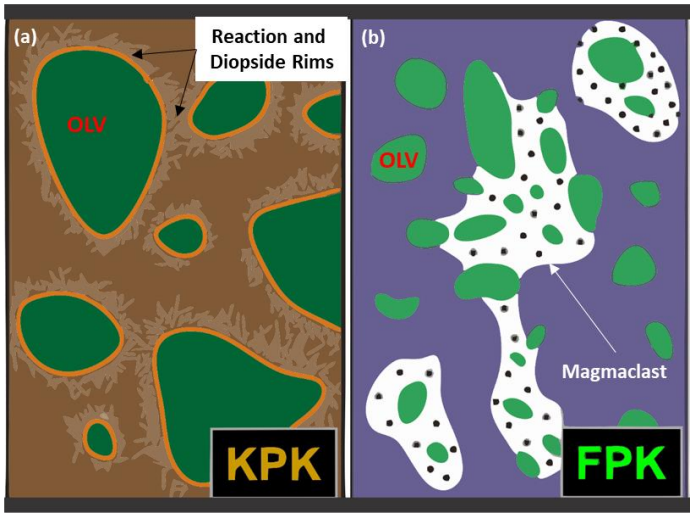

Figure 1.3 Magmaclasts from volcaniclastic kimberlites. Modified after Scott Smith et al. (2018).

1.3 Geological features of Class 1 kimberlites

Earlier kimberlite magmatic models and concepts were based on the evidence obtained from the deep mining of kimberlites in South Africa, as well as from subaerial and near-surface expression of kimberlite volcanism (Mitchell, 1986). Discoveries of kimberlite pipes in Canada over the last three decades and the work done by Field and

Scott Smith (1999), where they compared the kimberlite pipes of Canada and South Africa, led them to propose that the contrasting geology and the near-surface emplacement processes differ between pipe types and there exists a relationship between the pipe and the country rock geology. Kimberlite pipes were divided into three distinct classes: Class 1, 2, and 3 (Figure 1.4) based on the field investigations, and research done by Field and Scott Smith (1999) and Skinner and Marsh (2003).

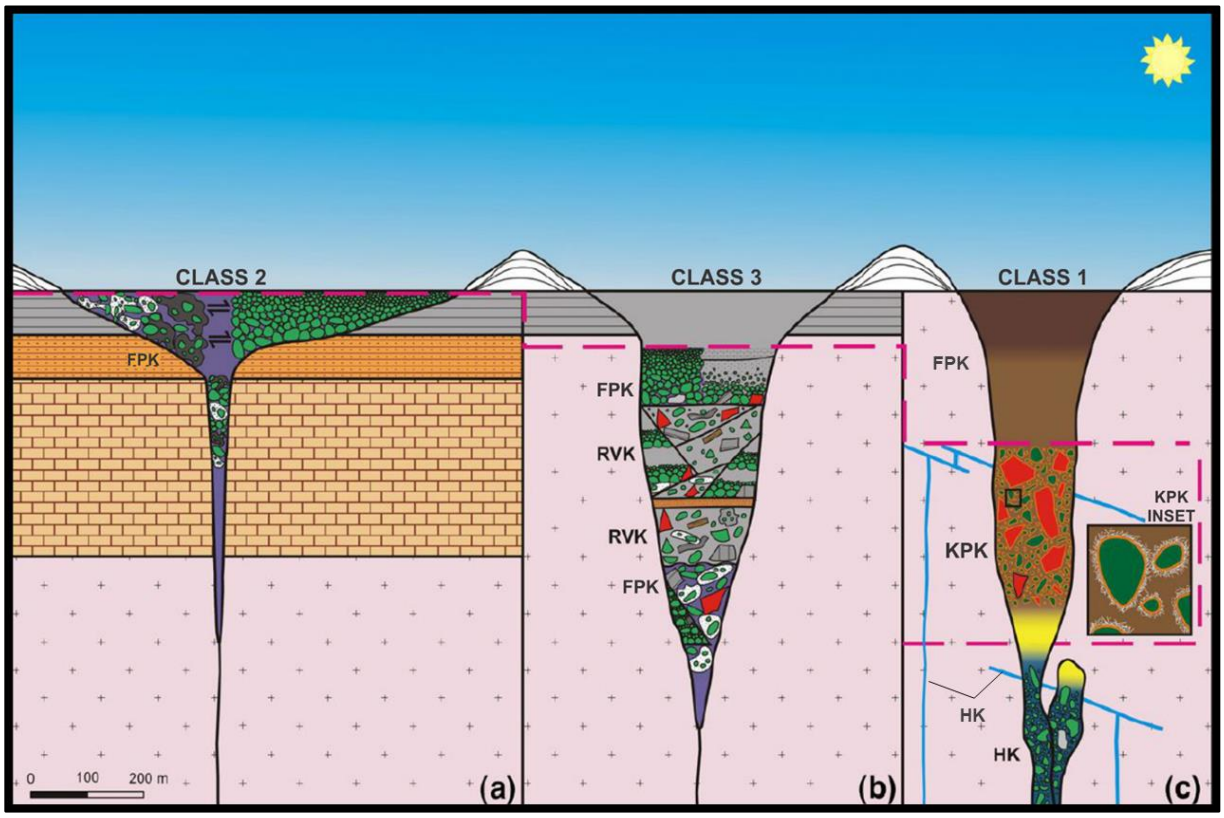

Figure 1.4: Three distinct kimberlite classes and the contrasting country rock geology in which the kimberlite magmas are emplaced. Pink dashed line indicates the present surface. Modified after Scott Smith et. al. (2013).

The class 1 pipe model is based on the kimberlite pipes found in South Africa (eg. Orapa, Kimberley), which are characterized by crater zone at the top, diatreme zone in the middle and the irregular shaped root zone at the bottom emplaced in a competent basement with little to no sedimentary cover (Figure 1.4c). Class 1 pipe type ranges from tens of meters to a few hundred meters horizontally and can extend up to 3 km vertically (Sparks, 2006). Common surface expression of the pipe shows near-circular to ellipsoidal form and is termed the crater zone (Sparks, 2006). The crater zone of the class 1 pipe is rarely preserved due to the erosion. Based on the limited studies

done, the rocks of the crater zone can be divided into lavas, pyroclastic and epiclastic rocks (Mitchell, 1986).

The conical diatreme zone is a long (1-2 km) body with the margins of the pipe dipping steeply (80˚-85˚) (Mitchell, 1986). The Kimberley-type pyroclastic kimberlites (KPKs) are the dominant rock types for the class 1 diatreme zones and the emplacement process for these rocks is described in more detail in *Section 1.5*. The deep and irregular shaped root zones, dikes and sill complexes host the hypabyssal kimberlites (HK). In few class 1 pipes around the world (Gahcho Kué, Angola, and South Africa), there exists a transition phase (KPK-HK) between the KPKs of the diatreme zone and the HKs of the root zone, and the transition zone can be up to tens of meters thick (Skinner and Marsh, 2004). Based on the petrographic analysis, the transition phase displays features of HKs as well as KPKs (Skinner and Marsh, 2004). Although the composition and textures of HKs are consistent across localities, the diatreme zone KPKs display a larger variability in appearance between pipe localities, while the overall mineralogy and textures are similar.

Class 2 pipes (Figure 1.4a) are characterized by a shallow crater zone with <500 m depth and the infill is dominated with fragmented pyroclastic kimberlite (FPK) (Skinner and Marsh, 2004). Class 2 pipes are emplaced in a competent basement with thick sedimentary cover and is the dominant pipe type found in the Canadian Prairies, northeast Angola, and Siberia (Skinner and Marsh, 2004). Class 3 pipes commonly contain horizontal to wedged shaped units of resedimented volcaniclastic kimberlites (RVK) and FPKs (Scott Smith, 2009). It is dominated by resedimented volcaniclastic kimberlites (RVK) along with lesser abundance of FPKs (Skinner, 2004). Class 3 pipe (Figure 1.4b) type has been discovered in Botswana; Lac de Gras, Canada; Aichal, Siberia; and Jwaneng, Botswana (Skinner et al., 2003). Low abundance of country rock xenoliths and evidence of extrusive infill in class 2 and 3 pipes indicates an open volcanic structure infilled by multiple magmatic eruptions (Scott Smith, 2006). The emplacement process of the FPKs found in class 2 and 3 pipes are well understood as they are the result of magma fragmentation, formation of pyroclasts and magmaclasts and their subsequent accumulation in the pipe (Scott Smith, 2006). Both pipe types

show evidence of discrete olivine grains, and the magmaclasts that are composed of serpentine or cryptocrystalline carbonate and olivine crystals (Scott Smith, 2006).

1.4 Mineralogy and textures of KPK

Much of the minerology and textures of the class 1 KPKs described below are based on the studies done on Canadian and South African kimberlites. Class 1 KPKs found elsewhere display similar mineralogical and textural features as well (see Das, 2013). KPKs are massive, unsorted, matrix-to-clast supported rocks that contain variable modal quantities and sizes of: xenoliths; autoliths derived from local country rocks and pre-existing kimberlites; abundant pseudomorphed olivine macrocrysts; lesser abundance of mantle derived macrocrysts (eg. Cr-garnet, Mg-ilmenite); and sub-spherical to elliptical magmaclasts set in a fine-grained interclast matrix with a distinctive microlitic component (Scott Smith et al., 2018). Subspherical shaped melt-bearing pyroclasts are generally composed of multiple olivine crystals or a single central olivine kernel surrounded by the primary microlitic groundmass in the pyroclasts consisting of spinel, monticellite, serpentine, apatite, phlogopite, perovskite, pseudomorphed melilite, chlorite and/or smectite (Scott Smith et al., 2018, Mitchell, 2009).

Pseudomorphed olivine and much of the components described above can be surrounded or overprinted by thin mantles dominated by microlitic diopside and/or phlogopite (Figure 1.5b) resulting in diffused rims of melt-bearing pyroclasts (Scott Smith, 2013; Mitchell, 2009). Microlitic diopside is a result of replacement of finer-grained primary matrix minerals within magmaclasts, or individual crystals within the primary serpentine matrix (Skinner, 2008). The interclast material between the melt-bearing pyroclasts is dominated by serpentine, microlitic diopside, phlogopite, and chlorite (Scott Smith et al., 2013; Mitchell, 2009). Due to secondary alterations pseudomorphed olivine, chlorite, and serpentinized interclast matrix can be completely altered or replaced by clay minerals and/or talc (Mitchell, 2009). Secondary carbonate veins are also observed in some KPK rocks (Figure 1.5a). Relative abundance of pseudomorphed olivine, and magmaclasts in KPKs are similar to HKs, except for the KPKs dilution by country rock xenolith (Mitchell, 2009). Melt-free discrete olivine crystals

are absent in KPKs but are observed in FALC kimberlites (after Field and Scott Smith, 1998).

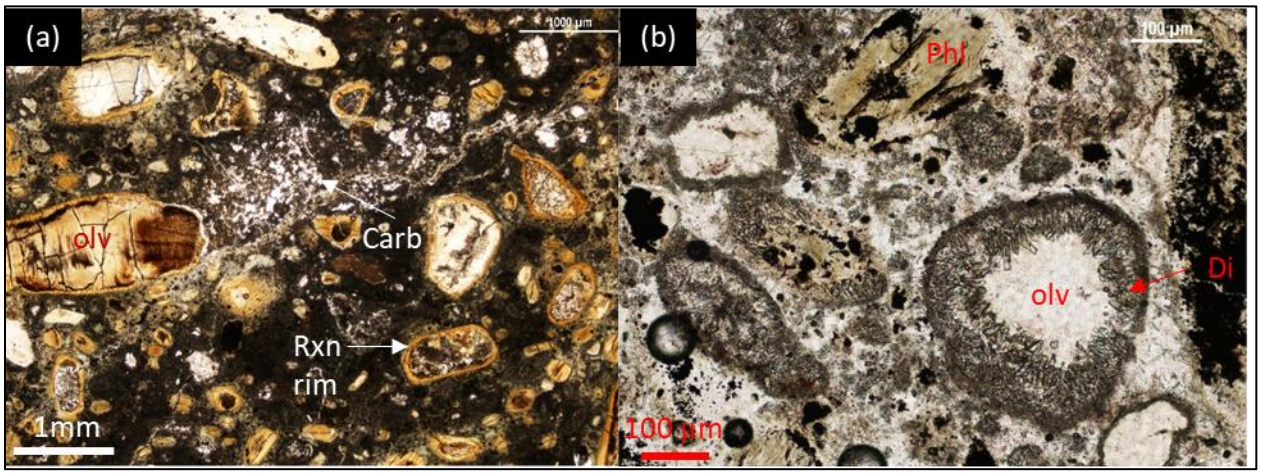

Figure 1.5: Microphotographs (in plane polarized light) of thin sections from KPK lithology in the class 1 kimberlite pipe from the Orapa kimberlite cluster, Botswana, South Africa at the depth of 57.5 m and 64.8 m respectively. (a) magmaclasts with kimberlite melt (dark brown), carbonate segregation (carb) and pseudomorphed olivines enclosed by reactions rims (rxn rim). (b) Diopside microlites (Di) around the rims of olivine, oxides (black), and phlogopite.

1.5 Models of formation of KPK lithology in Class 1

The emplacement process of class 1 kimberlite pipe diatreme zones has been of continued debate over the past two decades. Detailed studies and field investigations of kimberlite pipes in South Africa and Canada has led researchers to propose two distinct diatreme emplacement models. The first is the phreatomagmatic model of Lorenz (1975), which is still widely being used to explain some volcanic pipe formations. It is not an ideal model that can explain the nature of the majority of class 1 diatreme zones. Phreatomagmatism fails to explain the mineralogical and petrological differences of the different facies in the class 1 kimberlite pipes, and some kimberlite magmas have erupted through low permeability and low porosity crystalline basements with little to no sub-surface water presence (Skinner and Marsh, 2004).

The explosive volcanic model by Sparks et al. (2006) suggests the formation of the diatreme zone KPKs through explosive pyroclastic eruption with subsequent welding of the pyroclasts. The model envisions the formation of the diatreme zone from top down in four stages though extreme volcanic eruption. The initial stage involves initial cratering where the explosive magma rises to the surface along narrow fissures leading

to explosive eruptions. Rock-bursting, down-faulting, and crater-rim slumping in stage two leads to pipe excavation where pipe cross-section increases, and pipe deepens due to pressure differences. The pipe widening process comes to a halt once the eruptive magma mixture reaches one atmosphere pressure.

Pipe infill is achieved by pyroclasts derived from collapsing eruption conduit being trapped within the fluidized bed with denser particles sinking below, less dense particles and ash are flushed out of the system into an ash plume (Figure 1.6, Walters et al., 2006). Wall rock material is incorporated due to rock-bursts and slumping. Accumulation of hot pyroclastic material is achieved by high magma supply rates, which results in agglutination, sintering, lithification due to vapour phase crystallization, and elimination of pore space which results in gradational textures observed in the class 1 pipes (Sparks et al., 2006). The Interstitial serpentine present in the kimberlite melt represent the primary pore space and was infilled by hydrothermal magmatic fluids, whereas the diopside needles that fill the void space are a result of vapour phase crystallization under high temperature and sub-solidus conditions (Sparks et al., 2006). Post-emplacement, the hot pipe-infill experiences hydrothermal metamorphism due to meteoric water circulation and results in overprinting of olivines and country rock xenoliths by serpentine (Sparks et al., 2006; Walter et. al., 2006).

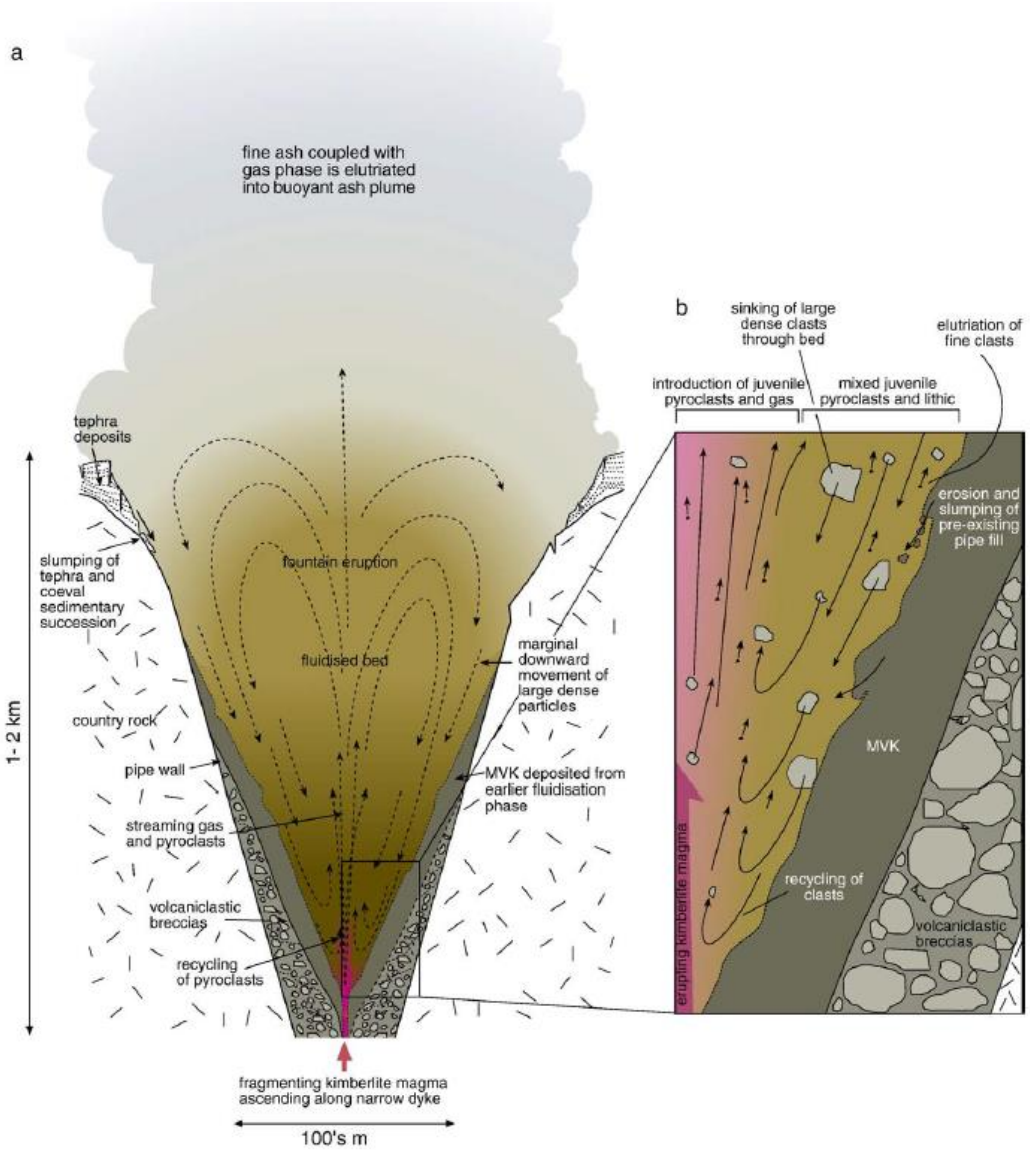

Figure 1.6: Role of fluidization in the formation of KPK. (a) Late stage eruption leads to pipe infill and the material includes the wall rock, kimberlite magma, and the KPK from the earlier fluidization event. During this stage, continuous supply of kimberlite magma leads to pyroclasts getting trapped and are fluidized by the on-going eruption of gas and pyroclasts. (b) Detailed image showing the inclusion of wall rock material due to rock-bursts and sorting of material due to density differences and slumping. From Walters et. al. (2006).

The subvolcanic-fluidization model of Clement (1982) envisions the formation and emplacement of diatreme zone KPKs as a result of in-situ crystallization, segregation, and magmatic exsolution of CO_2-rich volatiles of the HK magma. This model differs from the explosive volcanic model in that the diatreme zone is envisioned to be formed as a result of big-bang and from bottom-up (Clement, 1982). Initial

exsolution of melt-bearing pyroclasts is a direct result of depressurization due to the rising kimberlite magma (decrease in confining pressure) and leads to hydraulic fracturing of wall rock at depths of 2-3 km. At shallower levels, further volatile exsolution of pyroclasts is achieved due to crystallization and build-up of critical gas overpressures; this results in surface breach and leads to decompression and adiabatic cooling, which ends in explosive eruptions that generate compressive shock waves and leads to wall rock brecciation (Skinner, 2006).

Degassing results in downward propagation of a gas-front through the diatreme vent. Mixture of the interstitial gas and volatile-induced kimberlite magmatic phase results in a state of fluidization. During the explosion stage, large wall rock material falls back into the diatreme conduit and is mixed with the upward moving fluidized kimberlite mixture of solids and gas. Homogenization of the fluidized material is achieved by convective overturning (Skinner and Marsh, 2004). Microlitic diopside and serpentine crystallizes out of gas clouds formed from extensive exsolution at relatively low temperatures (<550 °C), which are particularly common at time of explosion (Skinner and Marsh, 2004).

$$\underset{\text{Montecellite}}{2CaMgSiO_4} + \underset{\text{Calcite}}{CaCO_3} + \underset{\text{Liquid}}{MgO + 4SiO_2} = \underset{\text{Diopside}}{3CaMgSi_2O_6} + \underset{\text{Gas}}{CO_2} \quad (1)$$

$$\underset{\text{Montecellite}}{CaMgSiO_4} + \underset{\text{Calcite}}{CaCO_3} + \underset{\text{Antigorite}}{Mg_{48}Si_{34}O_{85}(OH)_{62}} + \underset{\text{Liquid}}{2.32SiO_2} + \underset{\text{Gas}}{0.02O_2} \quad (2)$$

$$= \underset{\text{Diopside}}{CaMgSi_2O_6} + \underset{\text{Antigorite}}{0.98Mg_{48}Si_{34}O_{85}(OH)_{62}} + \underset{\text{Gas}}{CO_2} + 0.62H_2O$$

The above equations (HK (i) to KPK (ii) transition) describe the reactions resulting in exsolution of a CO_2-rich gas phase in addition to the decompressional degassing, which causes magma fragmentation and results in the mineralogical transition from HK-KPK, favouring the crystallization of primary diopside bearing assemblage (Skinner and Marsh, 2004; Skinner, 2008). The HK-KPK transition features described in this model were used to describe the observed features of diatreme zones in the Gahcho-Kue Mine, NWT, and the Wesselton Mine, SA Kimberlites (see Hetman et. al., 2004 and Mitchell et. al., 2009 for more detail).

1.6 Motivation for this study

Although the two models explain the kimberlite rock formation as a result of decompressional degassing and decarbonation reaction of the ascending magma, the models require large amounts of volatile (H_2O and CO_2) exsolution. Moreover, Hetman (2008) pointed out that the high degree of alteration experienced by the rocks in the kimberlite pipes may mask the important features related to pipe formation. The study of Moussallam et al. (2016) on volatile solubility shows that the volatile content of ascending kimberlite magma at shallower levels (2.5 km) ranges from 16 to 8%. Higher amounts of CO_2 will exsolve at shallower depths compared to H_2O which would likely exsolve at deeper levels. There is still uncertainty on the contribution of decarbonation reactions between the carbonate-rich kimberlite melt and the silicates of the country rock xenoliths. Additionally, an igneous process that would form textures similar to KPK have never been observed because there have been no modern kimberlite eruptions that were witnessed and KPK textures are not observed in other rock types. Although the temperatures of kimberlite melt generation are constrained between 1200-1400 °C at high pressures (> 2GPa) (Canil et al., 1999), the kimberlite melt generation and the reaction with wall rocks at lower pressures (<0.5 GPa) are poorly understood.

1.7 Objectives

This experimental study aims to examine the textures and the reaction minerals produced due to an interaction of a melt similar to an evolved kimberlite melt with different types of country rocks at low pressure conditions akin to low confining pressure at shallower depths in the diatreme zone (1-2 km) and examine to see if the produced textures are result of a closed or an open system. Fragments of basalt, granite, rhyolite, and andesite will be reacted with carbonate-rich kimberlite magma at 0.1 MPa and 500 MPa pressure conditions at temperatures of 800-1100 °C in order to explore the effects of temperature, H_2O, and CO_2. The observed reactions will be compared to the KPK textures of BK1 kimberlite from Orapa kimberlite cluster, Botswana and the kimberlites of Snap Lake and Gahcho Kue, NWT.

CHAPTER 2 – METHODS

2.1 Experimental Methods

2.1.1 Selection of starting material

The study used fragments of natural igneous rocks to represent crustal xenoliths of country-rocks entrained in kimberlite magma (Table 1). Two samples of fresh basalts from Hawaii and Iceland were used to examine the reaction between kimberlite melt and mafic rocks, such as the numerous xenoliths of Karoo basalts found in Orapa kimberlites, Botswana (Fedortchouk et. al., 2017). Canadian kimberlites, e.g. kimberlites on the Ekati Mine Property, contain xenoliths of granodiorite (Nowicki et. al, 2008). The experiments used granite as well as fine-grained rocks andesite and rhyolite to examine the kimberlite reaction with felsic and intermediate compositions. The rock samples were obtained from the rock library in the Department of Earth Sciences, Dalhousie University.

Table 2.1: Petrographic description of the xenoliths used in the study.

Rock Type	**Locality**	**Petrography**
Basalt (1)	Iceland	Vesicular basalt with minor hematite and ilmenite
Basalt	Hawaii, USA	Ca-rich tholeiitic basalt
Granite (402)	Concord, N.H., USA	Musc-Bio Granite, light grey, fine- to medium-grained
Rhyolite (444)	Chaffee County, Colorado, USA	Grey colour with quartz-feldspar phenocrysts
Andesite (447)	Mount Shasta, California, USA	Grey colour rock with hornblende phenocrysts

The study used three compositions representing evolved kimberlite melt (Table 2.2). The mixture (AN-1) is derived from the bulk rock composition of the Anaconda hypabyssal kimberlite (AN) forming a dyke in Ekati Mine property, NWT (Nowicki et al., 2008). The composition of the Anaconda dyke was selected as it did not breach the surface and did not lose volatiles (CO_2) nor produced fine ash material in an explosive eruption. In order to derive the composition of evolved kimberlite melt from the bulk composition of the Anaconda kimberlite, 50 vol% of the olivine (representing xenocrystal and phenocrystal macrocrysts) was subtracted from the bulk composition using the

estimate for macrocryst content from Scott Smith (2008). Cr_2O_3, P_2O5, and halogens (Cl, F) were not added to the synthetic mixture. Water was not added to the AN-1 mixture used in the experiments conducted at 0.1 MPa, but 10 wt% of de-ionized water was added with a micro-syringe in the high-pressure experiments.

In order to prepare the mixture for this study, the components were added as reagent grade oxides and carbonates (Table 2.3). CaO, MgO, Na_2O, and K_2O were added as the carbonates: $CaCO_3$, $MgCO_3$, Na_2CO_3, and K_2CO_3 (Table 2.3). CO_2 was added as carbonates as well ($CaCO_3$, $MgCO_3$, Na_2CO_3, K_2CO_3). The oxides and carbonates were weighed on an electronic balance. The weighted material was then mixed in an agate mortar and mixed using 95% ethanol. The mixture was then dried using a heat lamp and then stored in a closed glass vial which was placed in a desiccator.

Table 2.2: Starting compositions used in the experiments and composition of Anaconda and Leslie kimberlites form Nowicki et al. (2008). AN-1 and LS-26 are the synthetic compositions derived from the natural Anaconada (Sample: DDH96-17:170.4) and Leslie kimberlite (LDC-09:28.9) bulk rock composition.

Oxide, (wt%)	Anaconda Kimberlite	AN-1 Mixture	Leslie Kimberlite	LS-26 Mixture
SiO_2	24.6	7.13	30.1	14.37
TiO_2	1.1	2.82	0.61	-
Al_2O_3	1.8	4.66	1.4	3
Fe_2O_3	7.6	7.63	8.6	17.15
Na2O	0.5	1.30	0.1	0.22
K_2O	0.2	0.52	0.33	0.71
CaO	15.8	41.00	9.2	15.72
MgO	27.2	0.71	38.4	18.83
P_2O_5	0.6	-	0.5	-
Cr_2O_3	0.2	-	0.3	-
CO_2	15.2	34.23	2.9	29.7
H_2O	4.7	-		0.3
Total	**99.6**	**100.0**	**92.5**	**100.0**

Table 2.3: Preparation of 5g of AN-1 mixture.

Oxides (wt%)	Mixture Composition	Prepared Mixture
SiO_2	7.141	0.339
TiO_2	2.827	0.134
Al_2O_3	4.668	0.222
Fe_2O_3	7.640	0.363
Na_2CO_3	2.217	0.105
K_2CO_3	0.761	0.036
$CaCO_3$	73.258	3.480
$MgCO_3$	1.489	0.071
Total	**100**	**5**

The second composition is a mixture of Na_2CO_3 and $CaCO_3$ in equal weight proportions. This composition was selected as close to the eutectic in Na_2CO_3 – $CaCO_3$ system based on the Mitchell and Kjarsgaard (2008).

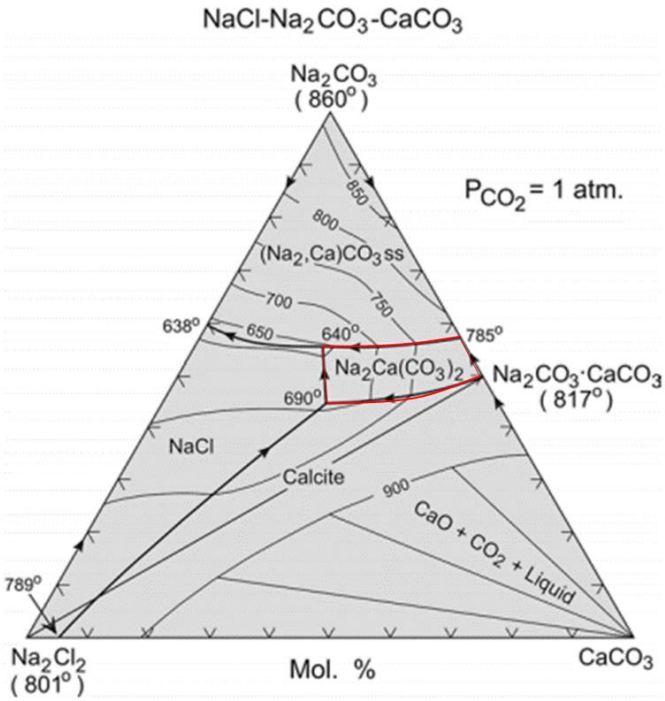

Figure 2.1: Na_2CO_3 – $CaCO_3$ – Na_2Cl_2 ternary diagram showing the phase relationship at 1 atm pressure of CO_2. Red area highlights the eutectic. From Mitchell and Kjarsgaard *(2008).*

The third mixture LS-26 was derived from the bulk composition of the pipe-infilling Leslie kimberlite located on the Ekati Mine property, NWT (Table 2.2). The preparation of LS-26 was similar to that of AN-1. First, 50 vol% of olivine was subtracted

and in order to account for the loss of volatiles, excess CO_2 was added to 26 wt% as carbonates ($CaCO_3$, $MgCO_3$, $CoCO_3$). Additional decarbonation step was added where $CaCO_3$, Na_2CO_3, and K_2CO_3 are heated to 900 °C. Cr_2O_3, TiO_2, P_2O_5, and halogens (CL,F) were not added to the mixture. The main difference between the AN-1 and LS26 compositions is the MgO content, which is 0.71 wt% and 18.83 wt% in AN-1 and LS-26, respectively.

2.1.2 Experimental conditions

The emplacement conditions and the cooling rates of the kimberlite magma are not well known. The estimates of crystallization temperature of kimberlite melt range from 1150-1300 °C for the phenocryst assemblage, and to to 600 °C for the groundmass (Fedortchouk and Canil, 2004; Mitchell, 1986). This study examined the upper range of the kimberlite temperature estimates but below the liquidus temperatures of the xenoliths employed. The anhydrous experiments at 0.1 MPa were done at 1100 °C to 900 °C for mafic and felsic xenoliths, respectively. Runs with H_2O at elevated pressures used 900 °C and 800 °C and <500 MPa pressure conditions for mafic and felsic xenolith experiments, respectively.

The pressure of 0.1 MPa was selected to examine reactions in the kimberlite pipes after emplacement. H_2O bearing runs were conducted at elevated pressures (200 MPa – 500 MPa) in order to prevent capsule explosion due to H_2O expansion. This allowed effect of H_2O on xenolith assimilation and reaction to be determined.

2.1.3 Sample and apparatus assembly

The experiments used two types of xenolith materials: cylindrical core and irregular fragments. A 2.8 mm dia. diamond curing drill bit was used to obtain 2-3 mm long and 2.5 mm dia. xenoliths of basalt and granite. Core sampling was replaced by xenolith fragments (approximately 1.5-2 mm in size) after two runs in order to achieve more uniform mixture interaction with the xenoliths. Experiments used 3 mm O.D., 0.127 mm wall thickness gold (Au) and platinum (Pt) capsules (Figure 2.2). Au was used in Fe-bearing experiments due to Fe loss in platinum capsules, and Pt was used in experiments at temperatures >1000 °C. The gold and platinum tubing was annealed in

a Ney Vulcun 3-550 furnace at 900 °C for four hours. Annealed tubings were quenched by placing them in an ethanol filled beaker and cleaned inside a Branson 1510 Ultrasonic cleaner.

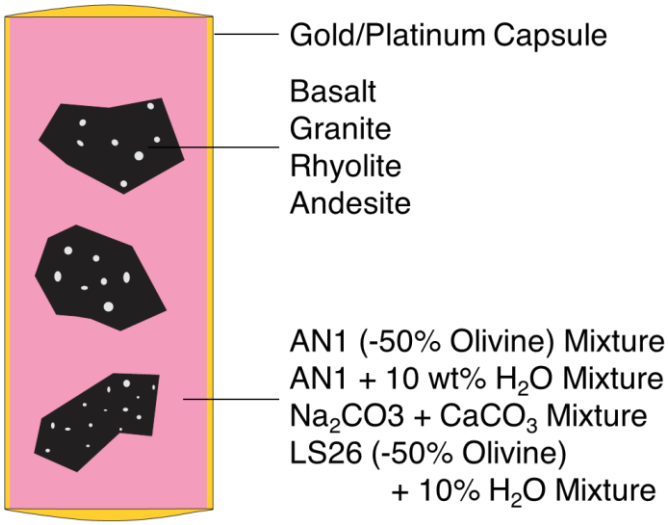

Figure 2.2: Cross-section of the 8 mm long capsule prepared for the experimental runs.

The base of the tube was welded first using a Lampert PUC-3 welder. The Kimberlite mixture was then added to the base, followed by the crushed pieces. The mixture/pieces addition process was repeated until the capsule was filled. The top of the capsule was then welded shut.

Table 2.4: Run conditions of experiments conducted for the study.

Runs	Apparatus	T (C)	P (Mpa)	Duration (hrs)	Xenoliths	Mix Composition
KM-1	Atmospheric Furnace	1000	0.1	4	Basalt Iceland	AN-1
KM-2	Atmospheric Furnace	1000	0.1	8	Basalt Hawaii	AN-1
KM-3	Atmospheric Furnace	1000	0.1	1	Granite	AN-1
KM-4	Atmospheric Furnace	1000	0.1	8	Basalt Hawaii	AN-1
KM-5	Atmospheric Furnace	1000	0.1	6	Basalt Hawaii	Na_2CO_3+$CaCO_3$
KM-6	Atmospheric Furnace	1000	0.1	6	Rhyolite	Na_2CO_3+$CaCO_3$
KM-7	Atmospheric Furnace	1100	0.1	4	Basalt Hawaii	AN-1
KM-8	Atmospheric Furnace	1100	0.1	4	Rhyolite	AN-1
KM-9	Piston Cylinder	1000	200	6	Basalt Hawaii	Na_2CO_3+$CaCO_3$
KM-10	Piston Cylinder	900	500	8	Basalt Hawaii	AN-1 + H_2O
KM-11	Piston Cylinder	800	500	8	Andesite	AN-1 + H_2O
KM-12	Piston Cylinder	900	500	8	Basalt Hawaii	LS-26 + H_2O
KM-13	Piston Cylinder	800	500	8	Andesite	LS-26 + H_2O

All the experiments for this study were conducted in the high-pressure lab at Department of Earth Sciences, Dalhousie University and run conditions varied between experimental runs (Table 2.4). H_2O-free experiments were conducted in a Lindenberg box furnace. Once the experiments run was over the capsules were quenched in a beaker filled with ethanol.

Rockland piston-cylinder apparatus was used to conduct experiments with H_2O at <0.5 GPa pressure where a 12.7 mm NaCl-Pyrex assembly was used (Boyd and England, 1960). For each experiment, the gold capsule infilling process was the same as the dry runs, but 10 wt.% de-ionized water was added using a micro-syringe to the capsules before welding shut. The capsules were inserted into a NaCl-Pyrex assembly (Figure 2.3) and wrapped with Pb-foil before being inserted into the pressure vessel. A brass base plug with a predrilled hole was placed inside a pyrex sleeve and was inserted on top of the assembly. The assembly is placed in a pressure vessel where the pressure to the assembly is applied with a tungsten-carbide piston. The 50 mm long thermocouple is then inserted through the brass plug down into the NaCl-pyrex assembly in order to obtain temperature readings. The temperature was monitored with a Eurotherm controller using $W_{95}Re_5$-$W_{74}Re_{26}$ thermocouple. Circulation of water through upper and lower steel plates was necessary in order to keep the pressure vessel cool.

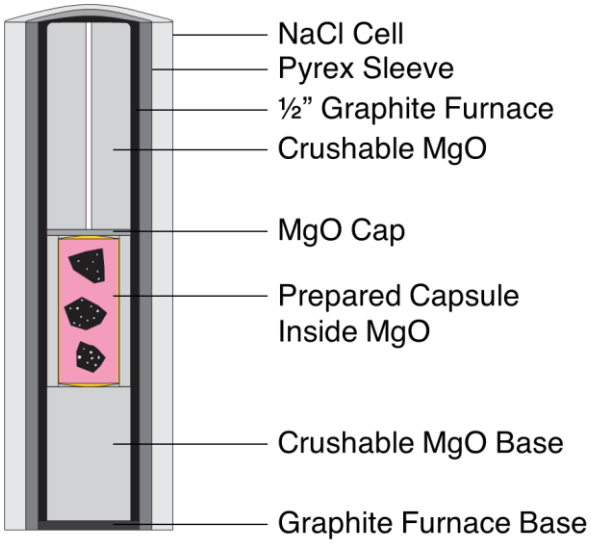

Figure 2.3: Cross-section of the assembly pieces for the Piston cylinder experiments. The assembly is approximately 31 mm tall.

The prepared assembly is pressured to ~ 250 Psi, before the temperature is ramped to 600 °C at 50°C/min and then held for 6 minutes. The assembly is then pressurized to the desired final pressure (~500 MPa) before ramping the assembly to the required temperature. The temperature remained constant throughout the experiment based on the thermocouple readings, but the pressure could drop and required no re-adjustments. Experiments were quenched by terminating power to the graphite furnace followed by slow depressurization.

Upon the completion of the experimental runs, the quenched capsules were set into a 1” diameter plastic mold and were back filled with epoxy. The capsules were grinded in dry conditions with a coarse grit (320) sanding paper to expose the material inside it. The exposed capsule interior was back filled with epoxy again to hold the material inside the capsule together. The grinding and cleaning process was repeated with medium (400) and fine (600) grit sanding paper and cleaned ultrasonically after each step. 1 µm and 0.3 µm micro alumina powder was used to polish the capsules and cleaned with acetone after every polish run. The molds were carbon coated before being analysed.

2.2 Orapa kimberlite samples

Polished thin sections from Orapa diamond mine were studied using a petrographic microscope in order to examine groundmass mineralogy and textures, as well as reactions around crystal xenoliths, and their evolution with depth. The Orapa kimberlite is part of the Cretaceous age Orapa kimberlite cluster overlying an Archean granite-gneiss basement (Chinn, 2013). The samples analysed for this study were obtained from drill-hole H002 (CK-A, MVK) with depth ranging from 34.5 m -75.5 m, and drill-hole H003 (CK-A, MVK) with depths ranging from 8.9 m – 142.7m of the Orapa BK01 kimberlite pipe (Chinn, 2013). The reaction textures and mineralogy around the country rock xenoliths were further studied and mapped using a scanning electron microscope (SEM) and the mineral phases were studied using a energy-dispersive spectroscopy (EDS).

2.3 Analytical methods

The mounts of the experimental run products and thin-sections of natural kimberlite samples were carbon coated and then analysed with SEM. The samples were studied using TESCAN Mira3-LM (FE-SEM) available at Saint Mary's University and Hitachi S-4700, cold field emission scanning electron microscope (FE-SEM) at the Faculty of Engineering, Dalhousie University. Compositional X-ray mapping on the run-products was done with JEOL 820 Superprobe electron microscope analyser (EMPA) housed at Dalhouse University. Both the energy dispersive x-ray spectroscopy (EDS) used in conjunction with the SEM and the EMPA bombard a high energy focused electron beam onto the sample surface to excite the electrons to a higher energy level and the x-rays are emitted in order to balance the energy difference between two electron states. Energy from each x-ray are measured by the EDS and the solid- state detector will then convert the x-ray energy to electrical signals. Table 2.5 shows the setting of each equipment used for EDS with a beam size of 1 µA and count time that varied between 20-30 seconds. Point and area analysis were done on the sample surfaces to obtain compositions of the mineral phases and the matrix.

Table 2.5: SEM and EMPA setting used for the analysis.

Analyser	**Voltage**	**Current**
TESCAN Mira3-LM FESEM	20 kV	17.0 µA
Hitachi S-4700 SEM	15 kV	17.0 µA
JEOL 820	15 kV	14.0 µA

CHAPTER 3 – RESULTS

3.1 Experimental Products

Table 3.1 provides a brief description of the experimental run results. All experiments preserved both mafic and felsic xenoliths and formed new phases in “kimberlite” matrix. Below, a detailed description is provided of the experimental products in the three run sets: 1) anhydrous runs at 0.1 MPa with AN-1 mixture, 2) anhydrous runs at 0.1 and 200 MPa with the carbonate mixture, and 3) H_2O-bearing runs with AN-1 and LS-26 mixtures at ~500 MPa.

Table 3.1: Results of the experimental runs.

Run	T (C)	P (Mpa)	Duration (hrs)	Xenolith	Mix Composition	Results	Comments
KM-1	1000	0.1	4	Basalt Iceland	AN-1	Loss of Material	Run Successful
KM-2	1000	0.1	8	Basalt Hawaii	AN-1	No Result	Capsule Melted
KM-3	1000	0.1	1	Granite	AN-1	Melting/Reaction	Run Successful
KM-4	1000	0.1	8	Basalt Hawaii	AN-1	Reaction	Run Successful
KM-7	1100	0.1	4	Basalt Hawaii	AN-1	Melting/Reaction	Run Successful
KM-8	1100	0.1	4	Rhyolite	AN-1	Reaction	Rhyolite Melted
KM-5	1000	0.1	6	Basalt Hawaii	Na_2CO_3+$CaCO_3$	No reaction	Capsule Exploded
KM-6	1000	0.1	6	Rhyolite	Na_2CO_3+$CaCO_3$	Reaction	Capsule Exploded
KM-9	1000	200	8	Basalt Hawaii	Na_2CO_3+$CaCO_3$	Melting/Reaction	Thermocouple Oxidation
KM-10	900	500	8	Basalt Hawaii	AN-1+10wt%H_2O	Reaction	Run problem with water, Re-ran it again
KM-11	800	500	8	Andesite	AN-1+10wt%H_2O	Reaction	Run Successful
KM-12	900	500	8	Basalt Hawaii	LS30+10wt%H_2O	No reaction	Run Successful
KM-13	800	500	8	Andesite	LS30+10wt%H_2O	No reaction	Run Successful

3.2 AN-1 composition

Petrography

Experiments with the AN-1 mixture (KM-1 – KM-4, KM-7, and KM-8 runs, Table 3.1) ranged in temperature from 1000 °C and 1100 °C at 0.1MPa involved both felsic (granite, and rhyolite) and mafic (basalt) xenolith reactions with the AN-1 mixture were compared to study the effect of temperature and to determine the resultant mineral phases. Figure 3.1 displays the first experimental run product in which the basalt xenolith was preserved and loss of AN-1 mixture adjacent to the xenolith during the polishing stage. AN-1 mixture shows a lighter zone (spectrum 1) and a darker zone (spectrum 2), where the former zone is more Fe-rich and the latter is more Mg-rich (Figure 3.1).

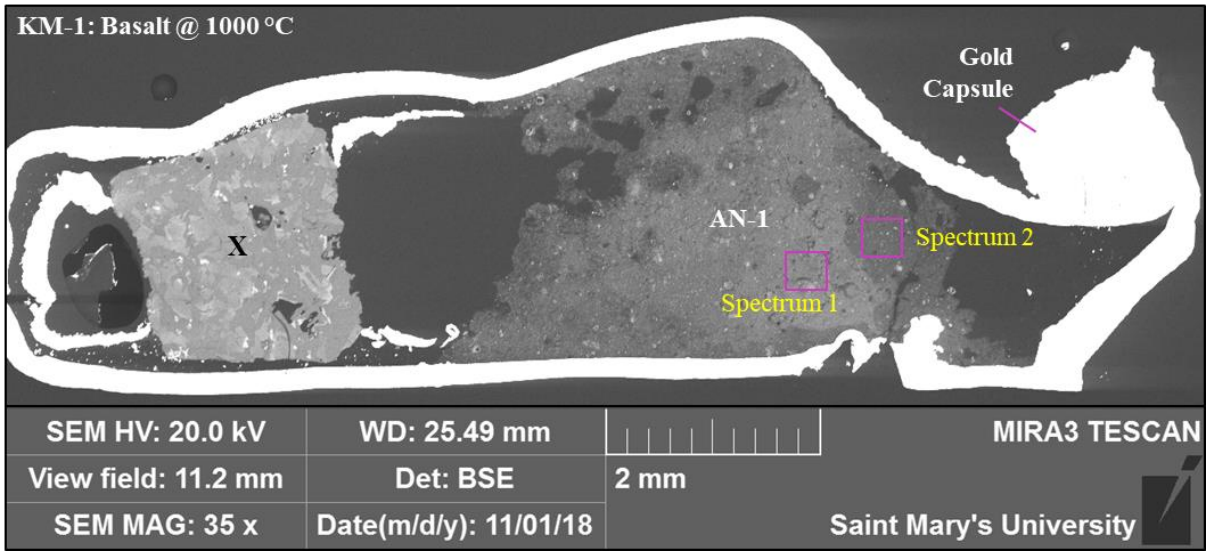

Figure 3.1 Overview of the first (KM-1) run product with basalt xenolith (X). Spectrum 1 and 2 shows the area where the composition of the AN-1 mixture was obtained.

KM-3 felsic run (granite xenolith at 1000 °C for 1 hour) product displays a great degree of interaction with the AN-1 mixture. Figure 3.2b shows assimilation of muscovite and partial melting resulting in diffused rims in the granitoid xenolith. KM-4 run product (basalt xenolith at 1000 °C for 8 hours) did not display any reaction with the xenolith as evident by the sharp contact between the xenolith and the AN-1 mixture (Figure 3.3b), although minor plucking of basalt pieces was observed. SEM analysis of the run product shows the presence of minerals such as perovskite, larnite, and minor calcite in the matrix in KM-3 and KM-4 run products.

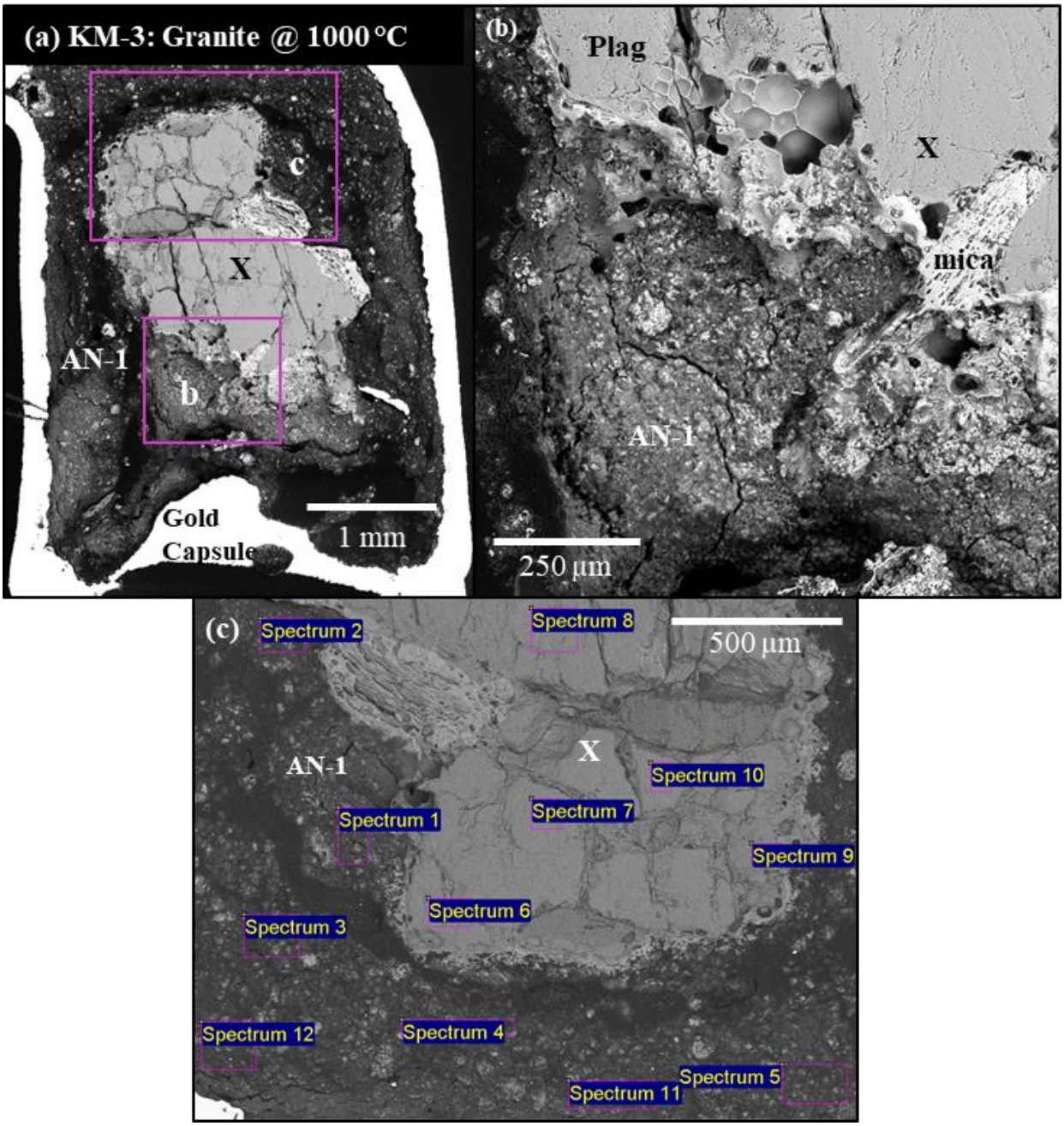

Figure 3.2: (a) Overview of KM-3 run product. (b) Shows the interaction between the granitoid xenolith (X) and the AN-1 mixture. (c) Spectrums 1-5, 11, and 12 were used to obtain area compositional analysis using the EDS.

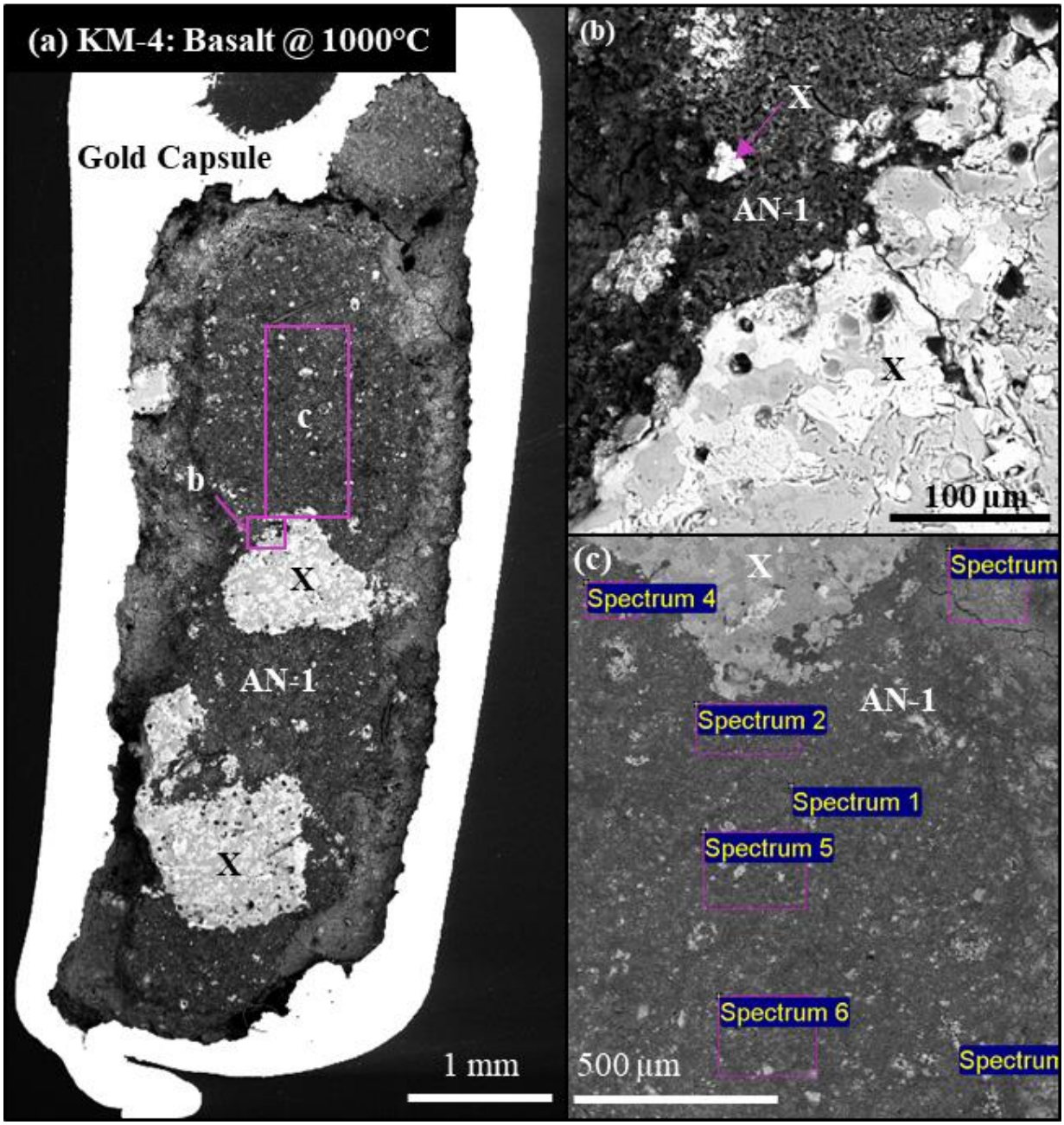

Figure 3.3: (a) Overview of KM-4 run product with basalt xenoliths (X). (b) Shows the interaction between the basalt xenolith and the AN-1 mixture. (c) Spectrums 2-6 were used to obtain area compositional analysis using the EDS (rorated 180°).

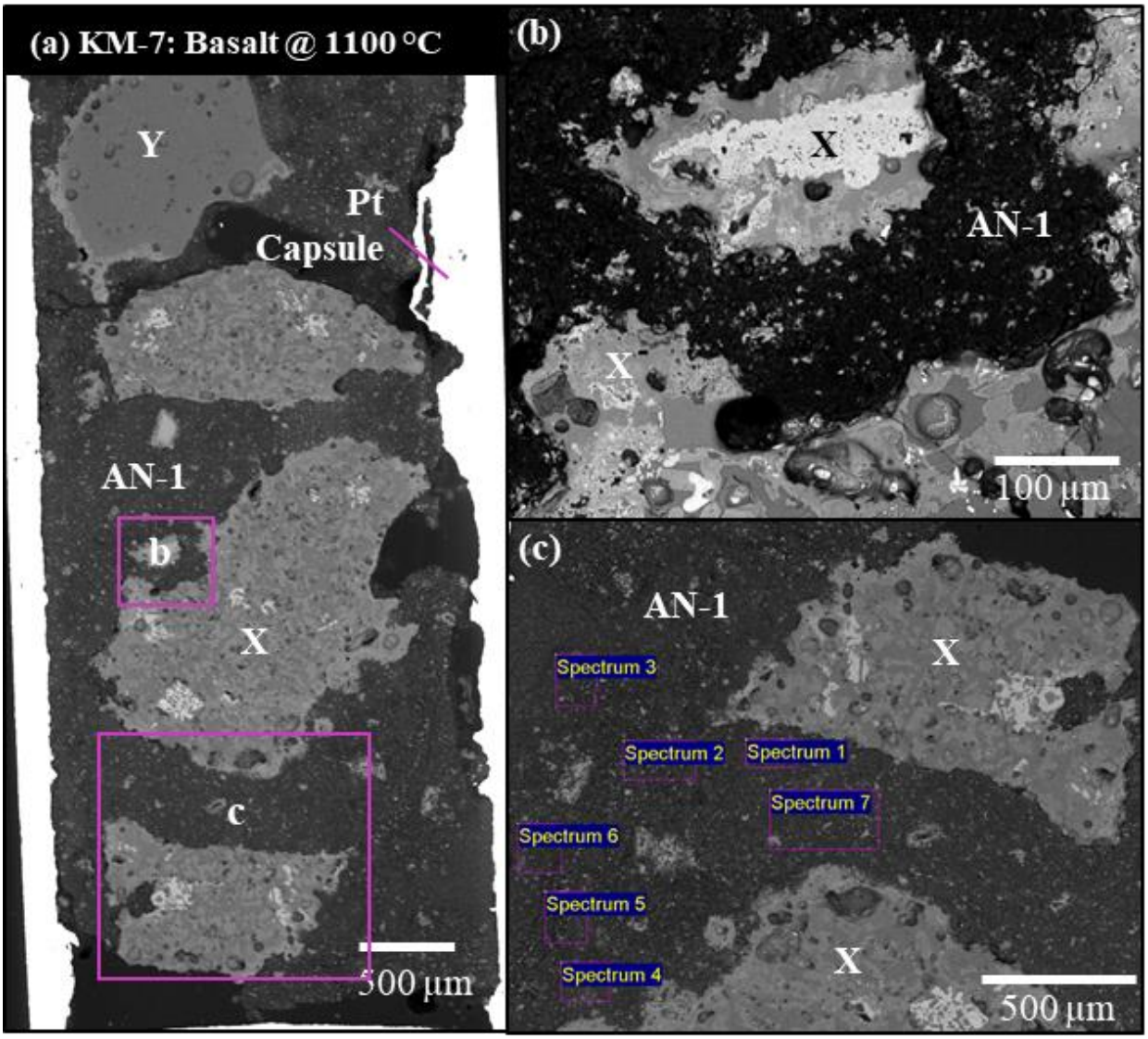

Figure 3.4: (a) Overview of KM-7 run product with basalt (X) and rhyolite (Y) xenoliths. (b) shows the interaction between the basalt xenolith and the AN-1 mixture. (c) Spectrums 1-7 were used to obtain area compositional analysis using the EDS.

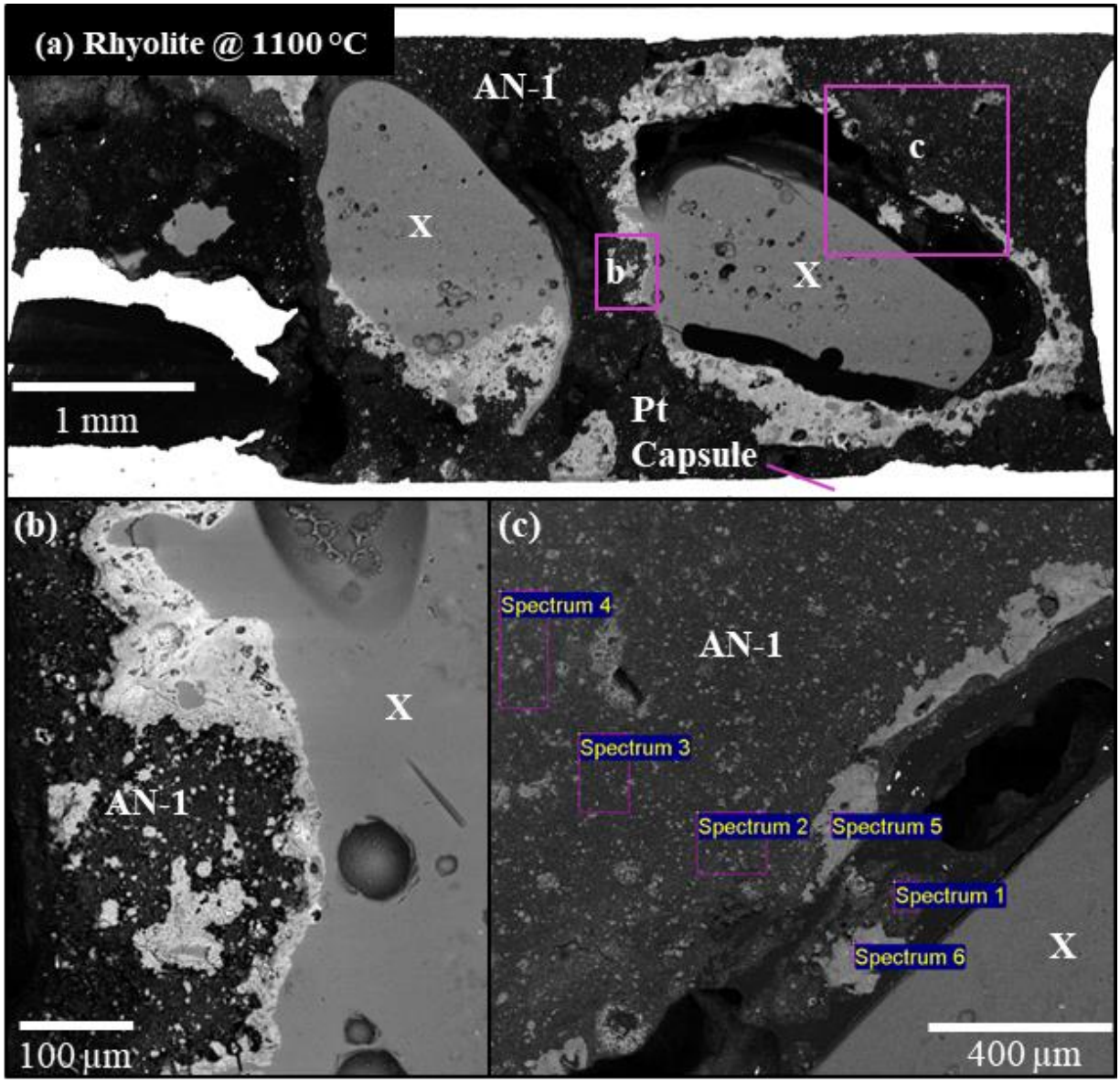

Figure 3.5: (a) Overview of KM-8 run product with rhyolite melt (X). (b) Shows the interaction between the rhyolite xenolith and the AN-1 mixture. (c) Spectrums 1-4 were used to obtain area compositional analysis using the EDS.

Experiments conducted at 1100 °C for 4 hours shows plucking of basaltic xenolith (KM-7, Figure 3.4b) and melting of the rhyolitic xenoliths (KM-8, fFgure 3.5a). The rims of the basalt xenolith (KM-7 run) appears more diffused compared to the basalt xenolith run experiment conducted at 1000 °C (KM-4). Melting of the rhyolite xenolith resulted in the formation of a thick reaction zone (Figure 3.5b). SEM examination of the KM-7 and KM-8 run products shows mineral phases such as perovskite, and larnite being observed in the matrix.

Matrix Composition

The average matrix composition from each run obtained using EDS is listed in Table 3.2 along with the starting composition. CO_2 was not analyzed in the experimental products, which should increase the relative concentrations of all other run products. Relative to the initial composition, there is an increase in SiO_2, Al_2O_3, CaO and MgO concentrations, and decrease in FeO concentration. K_2O and TiO_2 shows no notable change across experimental run products, whereas Na_2O concentration varies between runs.

Table 3.2: Average composition (wt%) of the experimental run products where 'n' indicates the number of compositional area analysis. See figures 3.1c - 3.5c for compositional areas. C.I. is the contamination index (See section 4.4).

Oxides (wt%)	**AN1**	**KM-1** ***(n=2)***	**KM-3** ***(n=7)***	**KM-4** ***(n=5)***	**KM-7** ***(n=7)***	**KM-8** ***(n=4)***
SiO_2	7.13	23.54	23.43	14.35	21.24	20.68
TiO_2	2.82	1.61	2.94	2.93	3.01	3.02
Al_2O_3	4.66	6.28	18.31	26.21	15.16	9.04
FeO	6.87	1.84	2.18	1.66	1.64	1.77
Na_2O	1.30	9.49	1.61	2.43	1.17	1.40
K_2O	0.52	0.73	0.41	0.22	0.20	0.20
CaO	41.00	50.79	47.89	50.66	54.56	60.72
MgO	0.71	5.72	3.22	1.59	3.04	3.18
CO_2	34.23	-	-	-	-	-
Total	100	100	100	100	100	100
C.I.	7.49	5.47	12.31	10.73	10.92	10.49

Ternary plots (Figure 3.6) compares the composition of the matrix from the runs with mafic and felsic xenoliths, and by varying temperature and run times. The plots show similar average composition of the matrix regardless of the composition of the xenoliths at the same temperature (e.g. KM-1-KM-3, and KM-7-KM-8). KM-4 run product composition is less differentiated than the other AN-1 runs and the composition is similar to the starting AN-1 composition other than the considerably high Al-content.

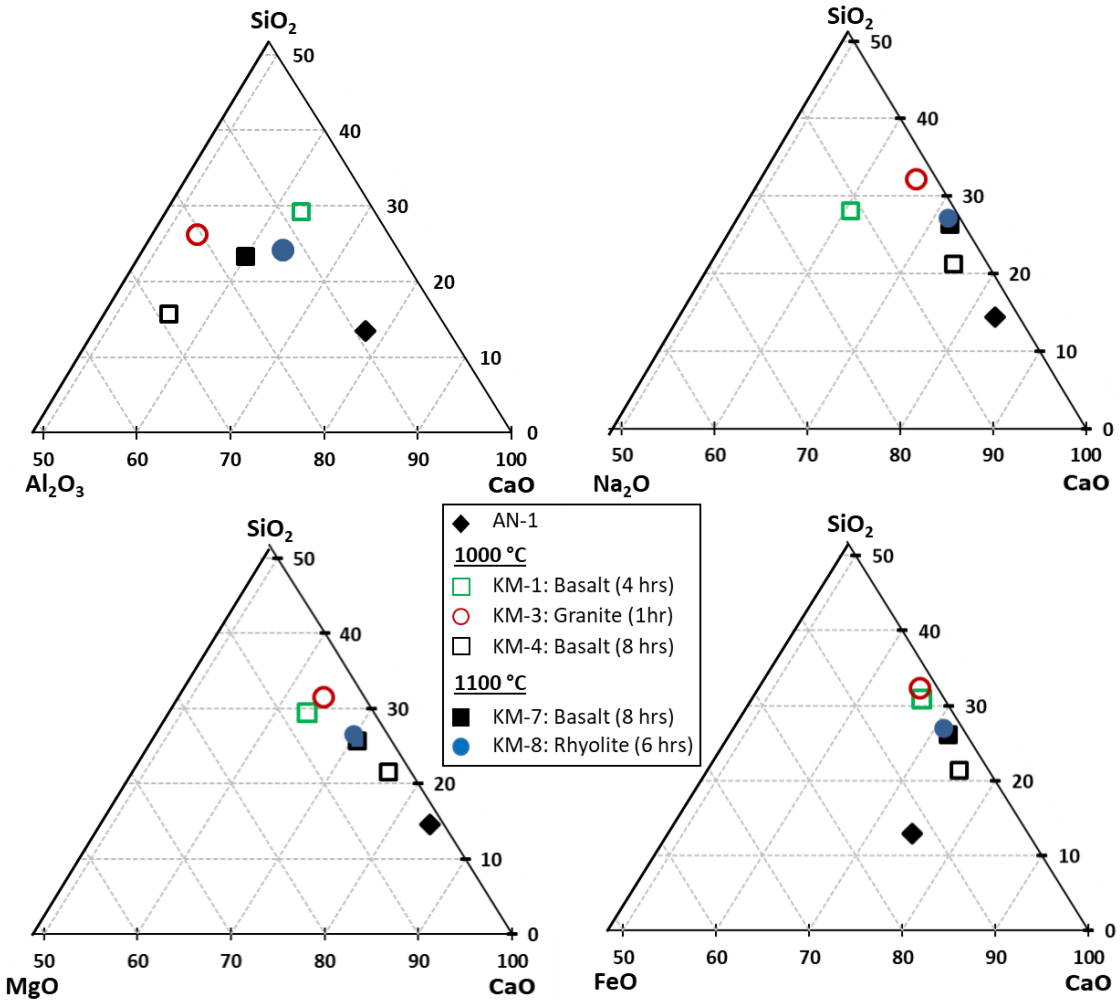

Figure 3.6 shows the ternary plots with average compositions of the AN-1 experimental run products. The concentrations are reported in wt%.

In order to study the compositional changes away from the xenoliths, distance profiles were constructed (Figure 3.7). Al_2O_3 and CaO shows an increase in concentration away from the xenoliths whereas the Si concentration decreases. TiO_2 shows a big positive spike in the middle followed by a sharp drop, but overall shows an increasing concentration trend. No apparent trend or relationship was observed between the KM-4 and KM-7 runs (basalt xenoliths at 1000 °C and 1100 °C, respectively).

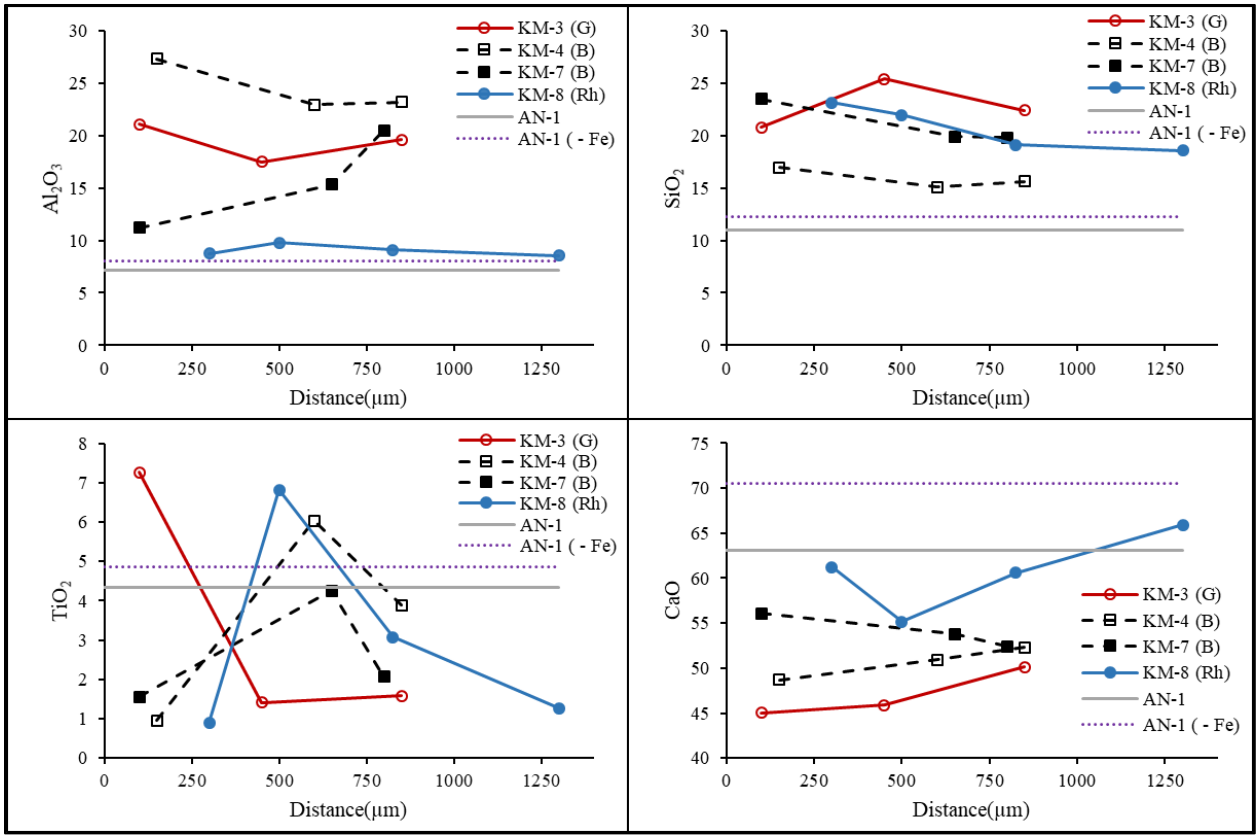

Figure 3.7: Compositional changes in the matrix as the distance from the xenoliths increases. o represents the felsic runs, and □ represents the mafic runs. An-1 (-Fe) indicates the AN-1 composition without iron. See table B1 in the appendix B for the compositions, and figures 3.1c - 3.5c for compositional areas

Compositional Mapping

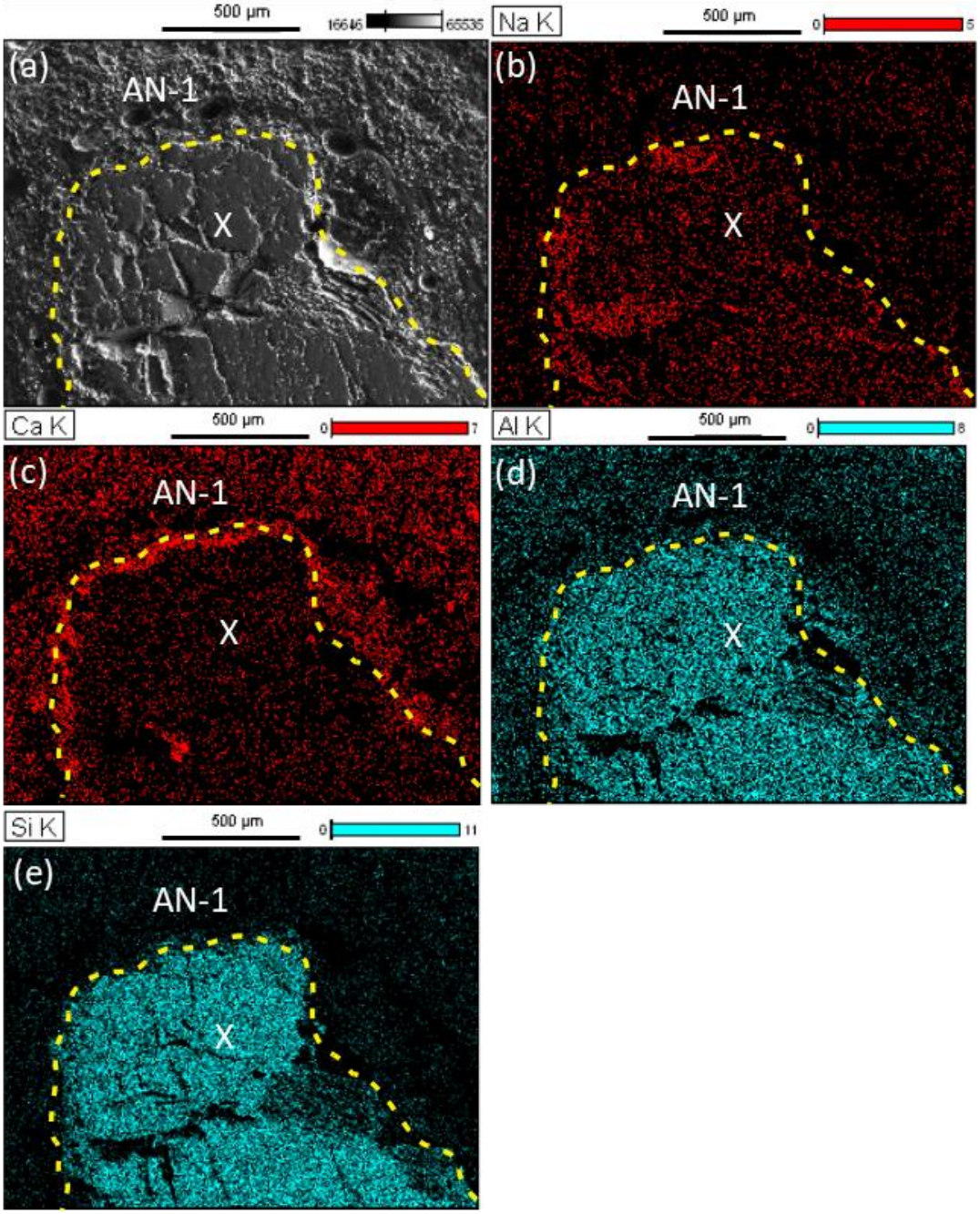

Figure 3.8: Compositional mapping of the KM-3 (at 1000 °C) run product performed using the EMPA. The dashed line marks the granite xenolith (X) boundary.

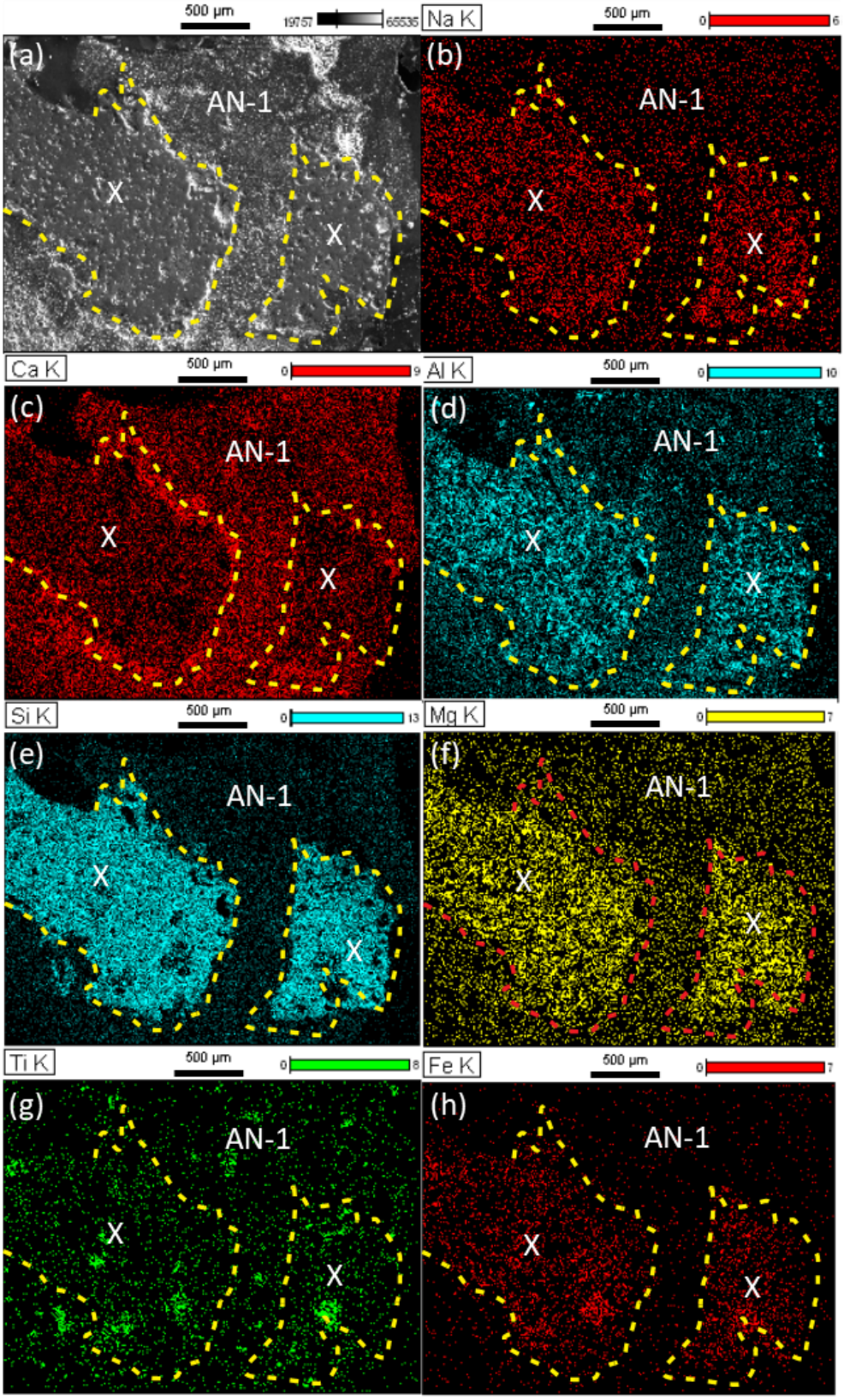

Figure 3.9: Compositional mapping of the KM-7 (at 1000 °C) run product performed using the EMPA. The dashed line marks the basalt xenolith (X) boundary.

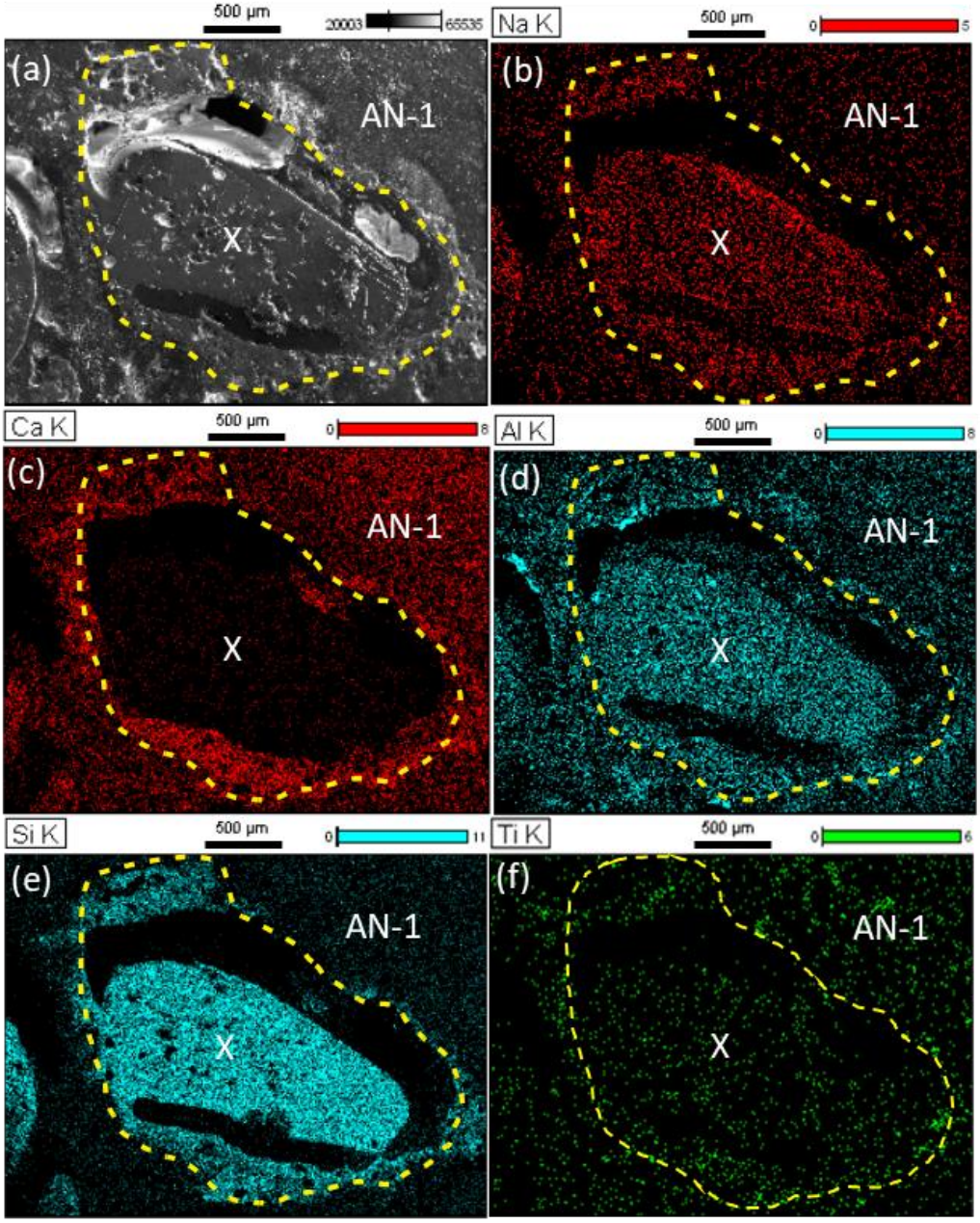

Figure 3.10: Compositional mapping of the KM-8 (at 1100 °C) run product performed using the EMPA. The dashed line marks the rhyolite xenolith (X) boundary.

Compositional mapping displayed diffusion of calcium and minor diffusion of sodium towards the rims of the xenoliths (Figure 3.8-10). The pattern was observed in both mafic and felsic runs. Titanium segregation due to development in mineral phase in the mixture as well as inside the xenoliths (KM-7). All other elements showed a more balanced spread of elements throughout the xenolith and the mixture.

3.3 $CaCO_3$ – Na_2CO_3 composition

Petrography

KM-5 and KM-6 experiments were conducted at 1000 °C for 6 hours with basalt and rhyolite xenoliths, respectively. Due to the explosion of the capsules KM-5 and KM-6, and the thermocouple oxidation of the KM-9 carbonate run, we were unable to obtain quantitative results of the mixture compositions. SEM analysis of the KM-5 and KM-6 experimental run product display reaction zones developing along the rims of the basalt xenoliths (Figure 3.11c), melting of the rhyolite xenoliths (Figure 3.12), and plucking of minor amounts of xenolith pieces along the rims (Figure 3.11c). No mineral phases were identified in the carbonate matrix due to loss of material.

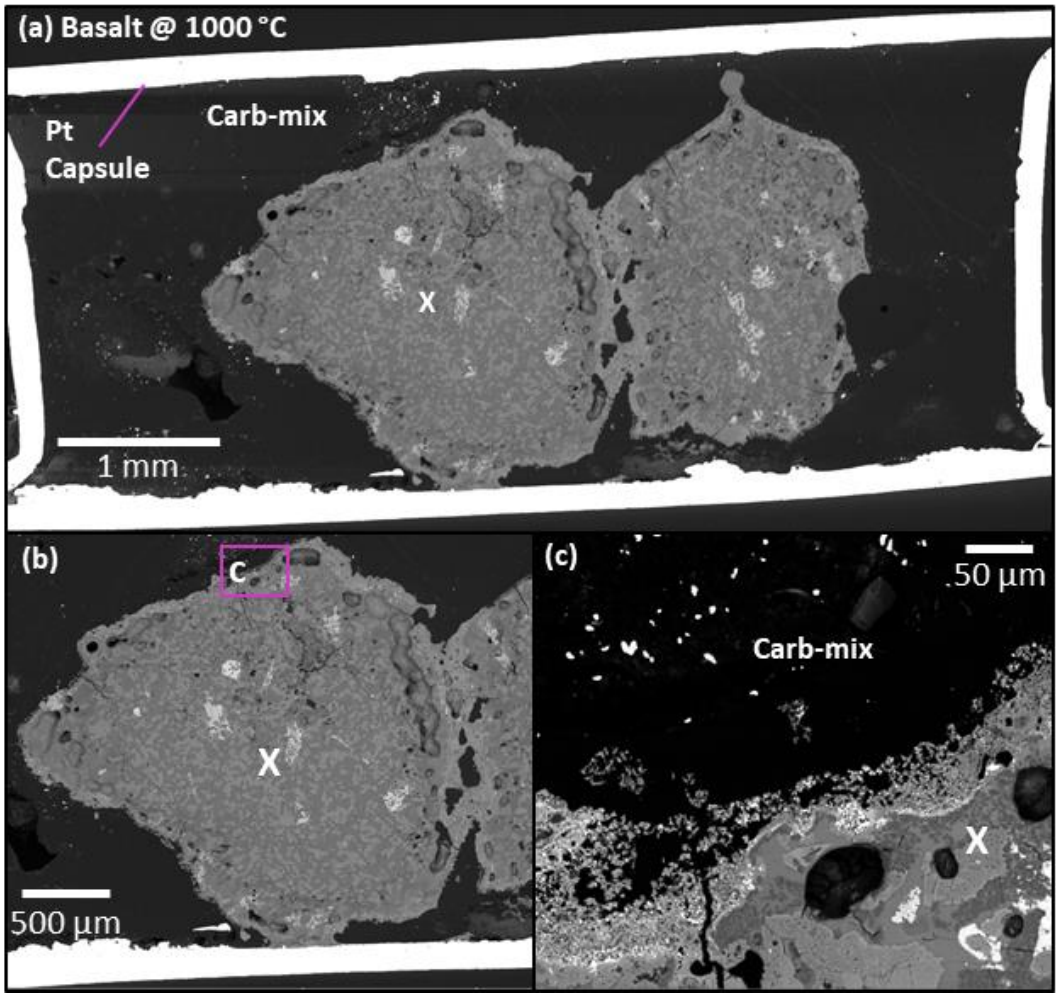

Figure 3.11: (a) Overview of KM-5 run product with basalt xenoliths (X). (c) Shows the interaction of the basalt xenolith with the carbonate mixture (Carb-mix).

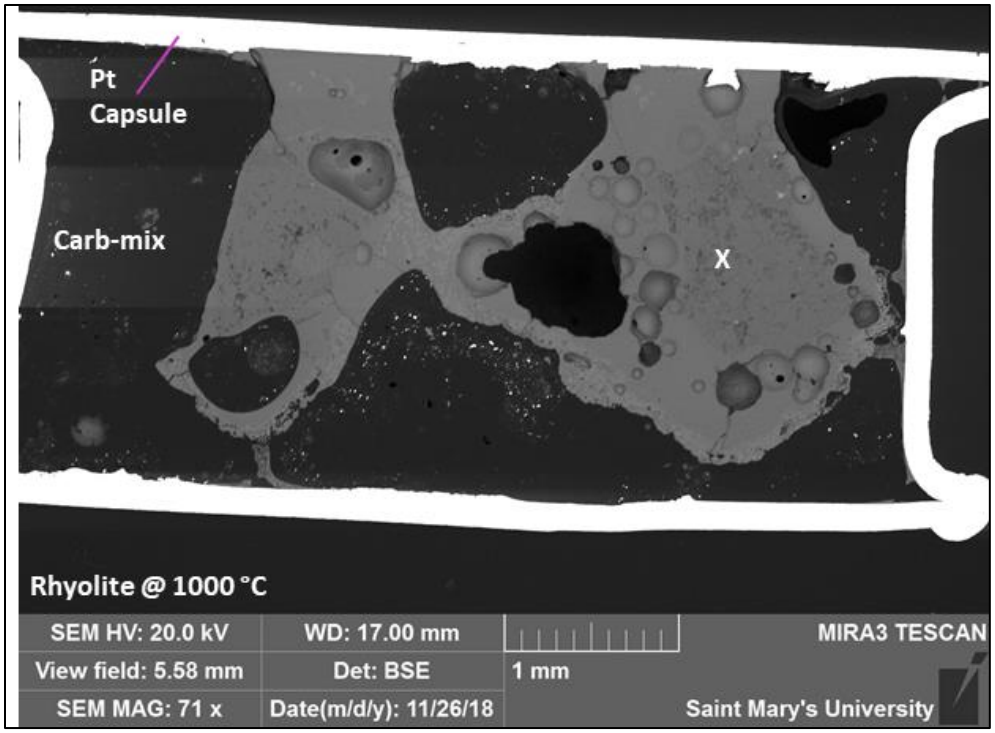

Figure 3.12: Overview of the KM-6 experimental run product with rhyolite xenolith (X) and carbonate mixture (Carb-mix).

Compositional Mapping

The compositional mapping analysis displayed the diffusion of calcium and sodium towards the rims of the xenoliths (Figure 3.13b,c). Aluminum and Silica appears to have concentrated towards the centre of the rhyolite melt (Figure 3.13d,e).

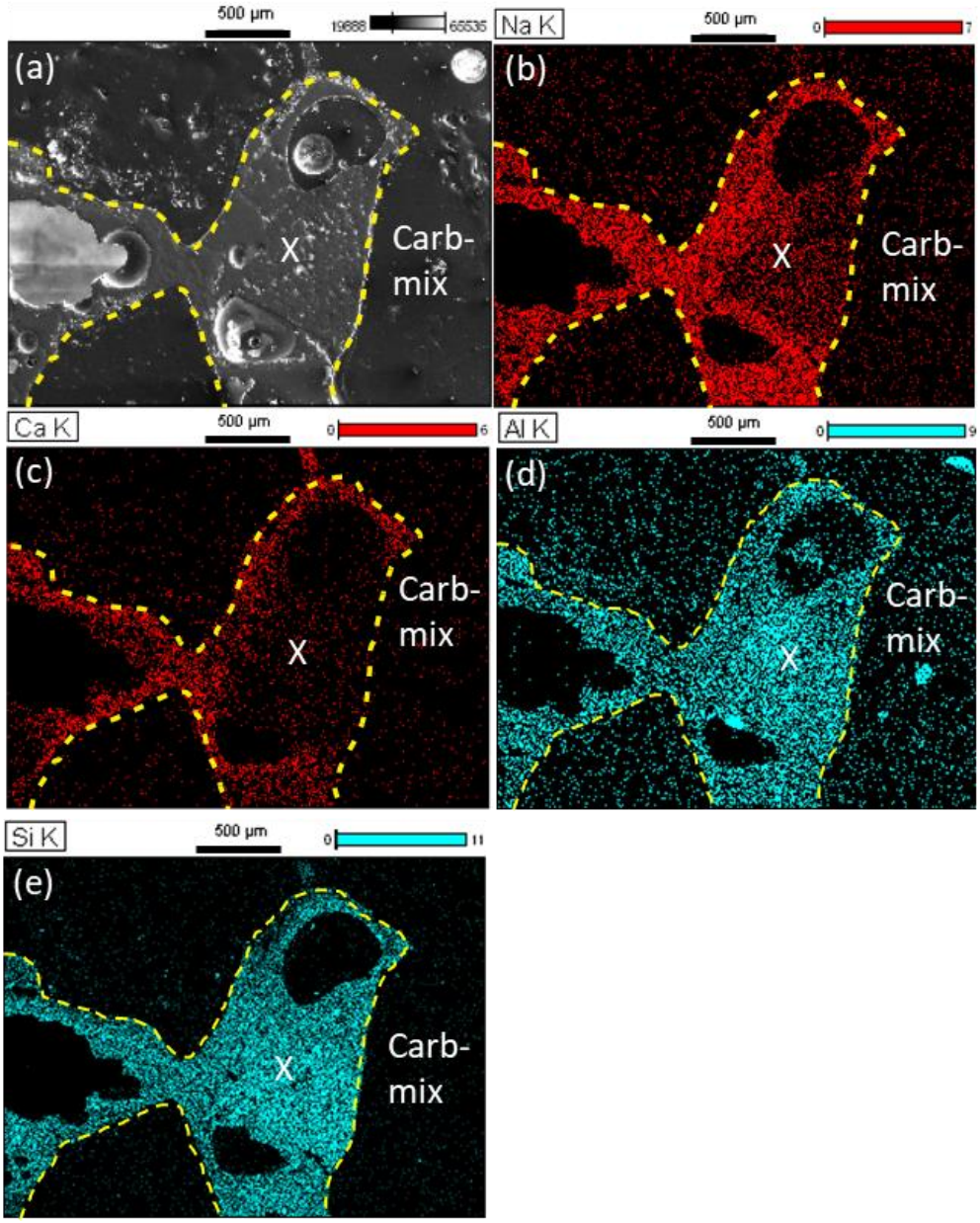

Figure 3.13 *Compositional mapping of the KM-6 (at 1000 °C) run product performed using the EMPA. The dashed line marks the rhyolite xenolith (X) boundary*.

3.4 AN-1 + H_2O composition

Petrography

The piston cylinder experiments KM-10 (basalt) and KM-11 (andesite) were conducted at ~500 MPa for 8 hours at 800 °C and 900 °C, respectively. Figure 3.14a and 3.15a shows black holes filled with epoxy (originally voids) indicating that water was retained during the experimental runs. The KM-10 experimental run product did not

display any interaction between the basalt xenoliths and the AN-1 + H_2O mixture. Partial melting of mineral phases was observed close to the rims of the basalt xenoliths (Figure 3.14b). KM-11 run product displayed minor interaction with the AN-1 + H_2O mixture and shows development of minor reaction zone along the andesite xenoliths (Figure 3.15b). SEM analysis of the run product shows the presence of perovskite and other minor calc-silicate minerals such as wollastonite, and melilite in the matrix.

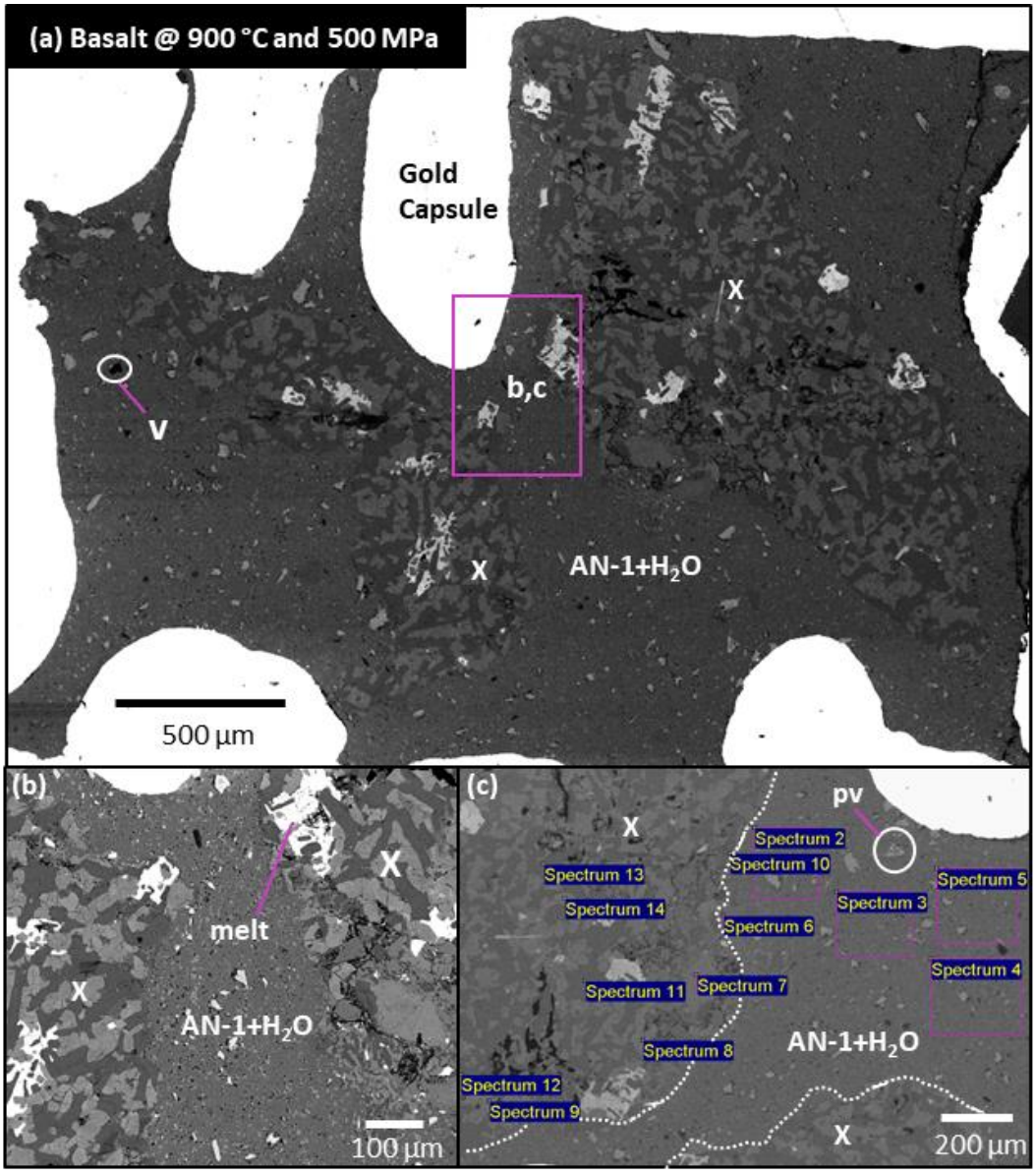

Figure 3.14: (a) Overview of the KM-10 run product with basalt xenoliths (X) and voids (v) filled with epoxy. (b) Shows the interaction of basalt xenolith and the matrix along with the partial melting of mineral phases (melt). (c) Spectrums 2-5 were used to obtain area compositional analysis using the EDS and perovskite (pv) mineral. Dotted line indicates the xenolith boundary.

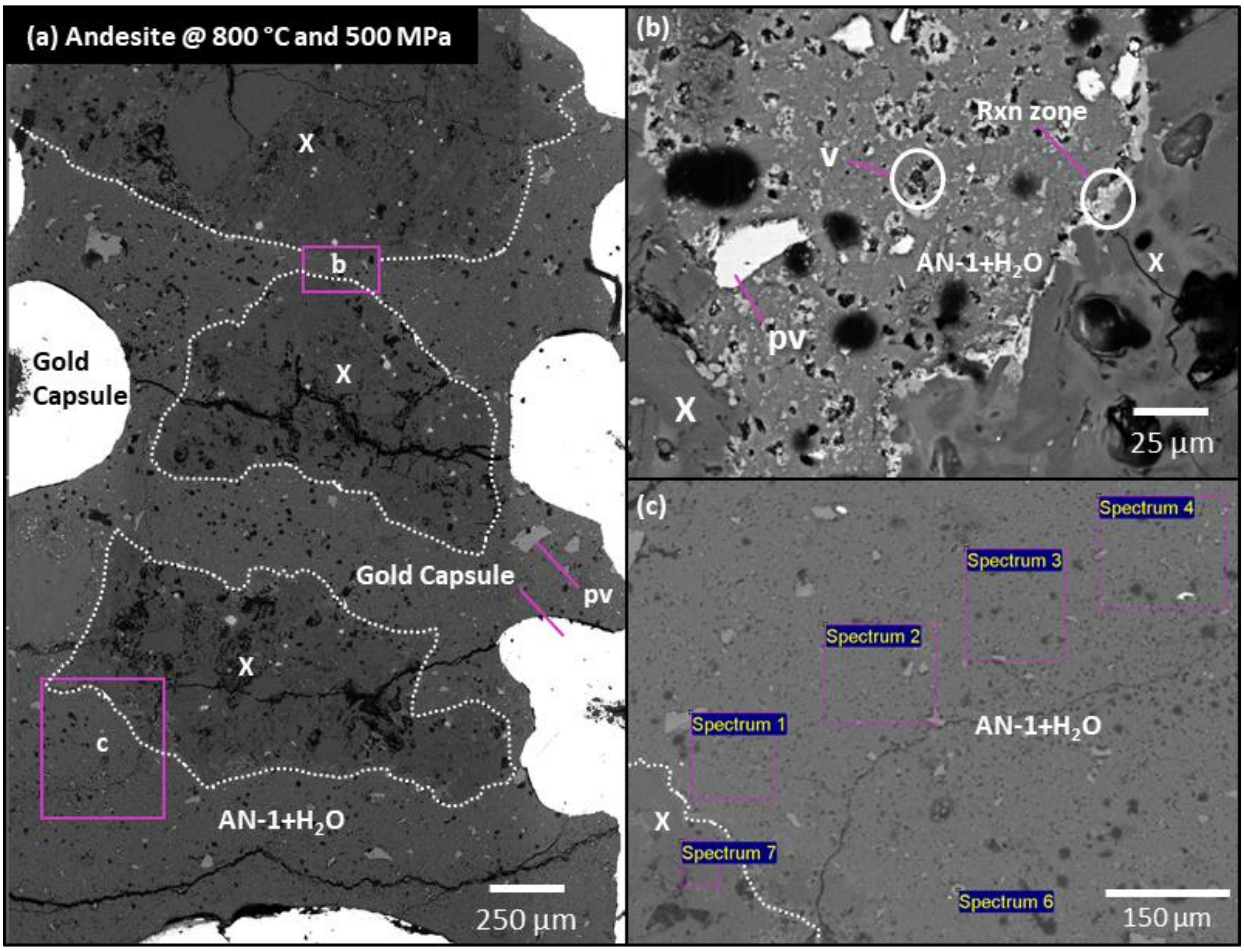

Figure 3.15: (a) Overview of the KM-11 run product with andesite xenoliths (X) and the perovskite (pv) minerals. Dotted line indicates the xenolith boundary. (b) Shows the interaction of andesite xenolith and the matrix, perovskite (pv) minerals, and voids (v) filled with epoxy. (c) Spectrums 1-4 were used to obtain area compositional analysis using the EDS.

Matrix and Xenolith Compositions

The average matrix composition from each run obtained using EDS is listed in Table 3.3 along with the starting composition. Again, CO_2 was not analysed in the experimental products, which should increase the relative concentrations of all other run products. There is an increase in SiO_2, MgO and CaO concentrations, and decrease in K_2O and FeO concentration. Al_2O_3, TiO_2, and Na_2O show an increase in concentration for the basalt run (KM-10), and decrease in concentration for the andesite run product (KM-12).

Table 3.3: Average composition (wt%) of the experimental run products where 'n' indicates the number of areas analysed. See Figures 3.4.1c and 3.4.2c for compositional areas. C.I. is the contamination index (See section 4.4).

Oxides (wt%)	AN1	KM-10 *(n=5)*	KM-11 *(n=4)*
SiO_2	7.13	23.44	15.88
TiO_2	2.82	4.09	2.89
Al_2O_3	4.66	8.57	3.27
FeO	6.87	1.09	1.27
Na_2O	1.30	3.43	1.14
K_2O	0.52	0.10	0.24
CaO	41.00	57.80	73.47
MgO	0.71	1.51	1.85
CO_2	34.23		
Total	100	100	100
C.I.	7.49	20.73	8.71
ln Si/Al	0.30	0.88	1.46

Table 3.4: Shows the pyroxene (figure 3.4.1c, spectrums 9, 8, 14) and albite (Figure 3.4.1c, spectrum 12, 11, 13) compositions from rim to the core of the basalt xenolith pieces in the run products (KM-11).

Pyroxene (wt%)	15 µm	20 µm	455 µm
SiO_2	52.75	52.28	53.7
TiO_2	0.88	1.21	0.7
Al_2O_3	2.11	2.09	1.05
FeO	11.47	12.57	20.33
Na_2O	0.59	0.41	0.09
CaO	18.41	17.43	4.17
MgO	13.64	13.95	19.53
MnO	0.11	0.17	0.36
Total	**100**	**100**	**100**

Albite (wt%)	30 µm	350 µm	560 µm
SiO_2	53.07	52.39	53.33
TiO_2	0.14	0.05	0.04
Al_2O_3	28.77	29.78	28.5
FeO	0.96	0.94	0.81
Na_2O	4.47	3.65	4.51
K_2O	0.29	0.14	0.48
CaO	12.34	13.05	12.4
MgO	0	0	0
Total	**100**	**100**	**100**

Table 3.4 shows a change in the pyroxene composition as the distance from the AN-1 + H_2O mixture increase. Concentration of MgO, and FeO increase, whereas the CaO and Al_2O_3 concentration decreases. In Albite, there is no notable changes in the concentrations from rim to core. Si concertation does not change from rim to core in pyroxene and albite.

Ternary plots (Figure 3.16) compares the composition of the matrix from the runs with mafic and felsic xenoliths, with 10 wt% water added, 500 MPa, and at 800-900 °C. The plots show the average andesite run product composition (KM-11, table 3.3) is much more similar to the original AN-1 composition whereas the basalt run product composition (KM-10, table 3.3) appears to be more SiO_2 and Al_2O_3 rich compared to other two.

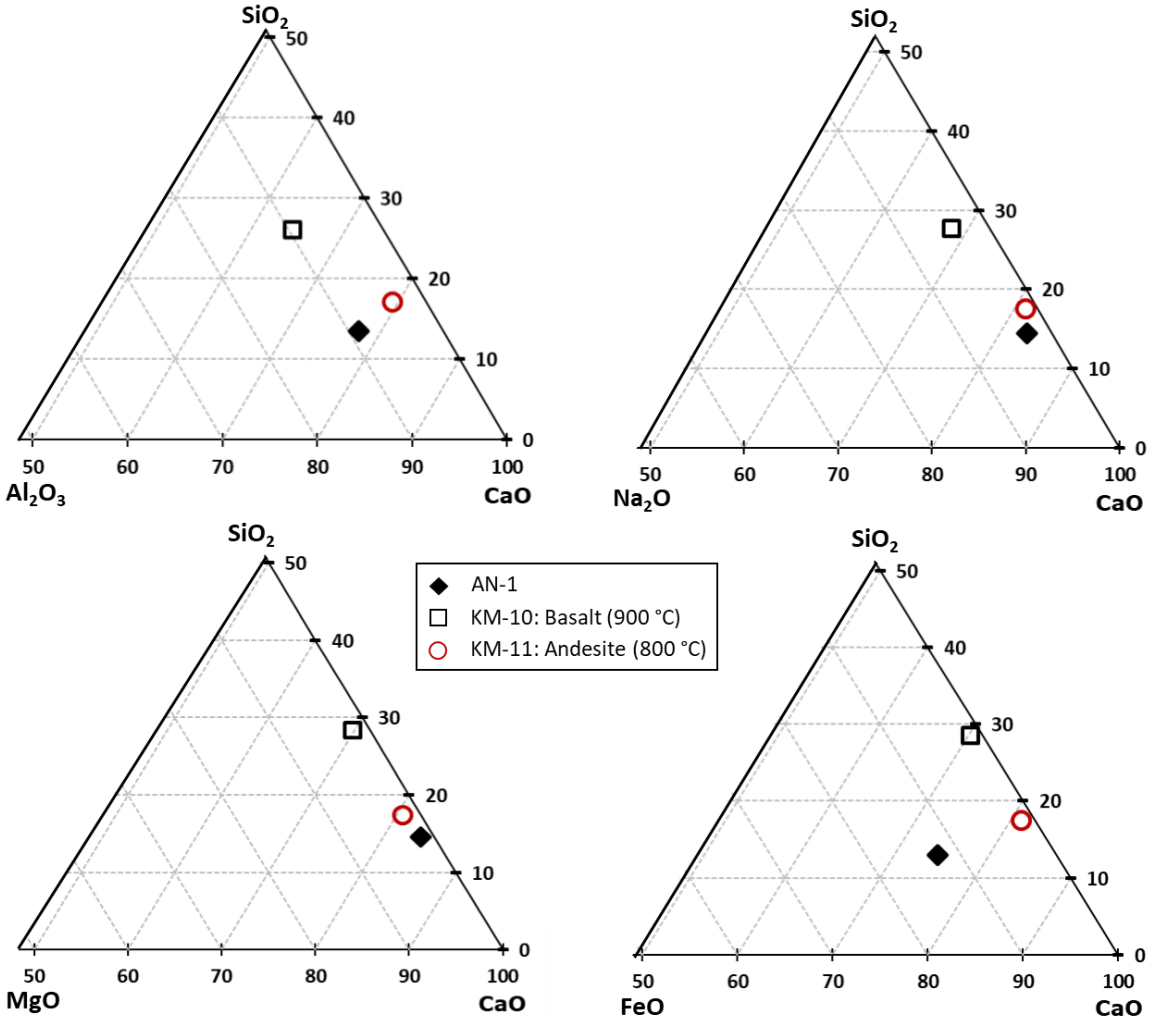

Figure 3.16 shows the ternary plots with average compositions of the experimental run products along with AN-1 mixture composition. The concentrations are reported in wt%.

Distance profiles of the experimental run products of KM-10 and KM-11 (Figure 3.17). Al shows an increase in concentration away from the xenoliths for both andesite and basalt run products, whereas CaO shows same trend irrespective of the xenoliths (basalt xenoliths at 1000 °C and 1100 °C, respectively). There is only minor change in

SiO_2 concentration overall and TiO_2 shows a decrease in concentration for both basalt and andesite runs.

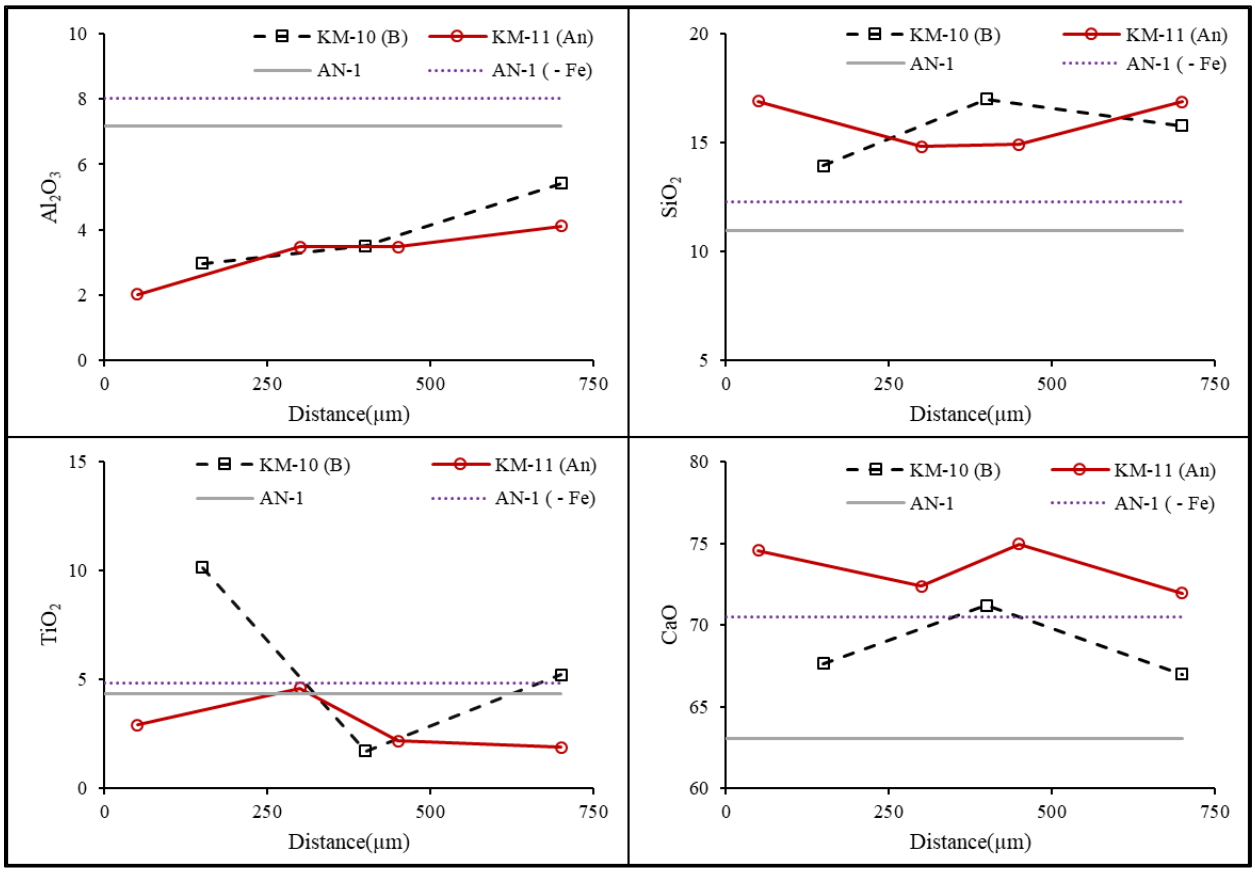

Figure 3.17: Distance profiles of the major elements from the AN-1+10wt% H_2O experimental runs. An-1 (-Fe) indicates the AN-1 composition without iron. See table B2 in appendix B for the compositions, and Figures 3.14c - 3.15c for compositional areas

Compositional Mapping

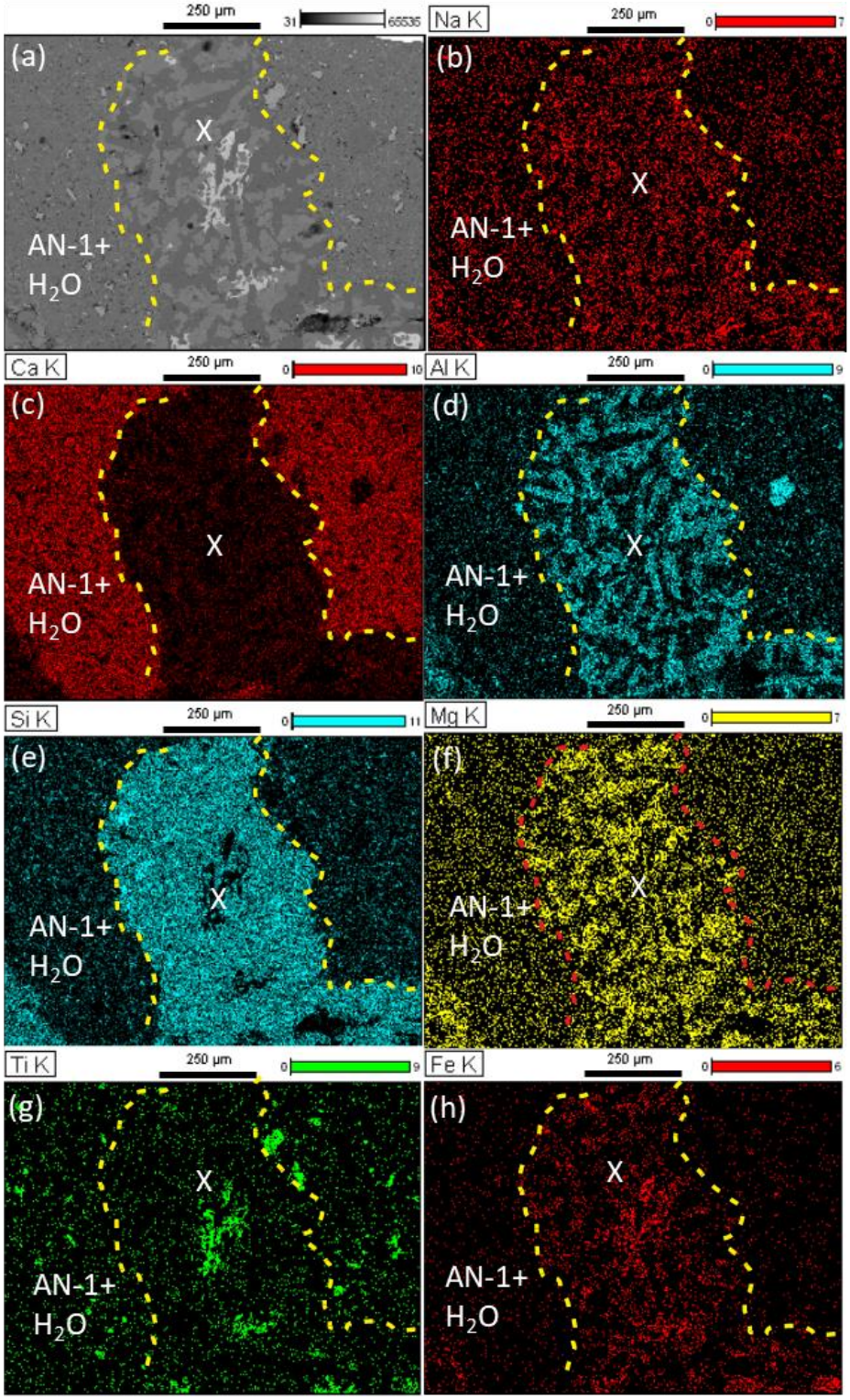

Figure 3.18: Compositional mapping of the KM-10 (at 900 °C and 500 MPa) run product performed using the EMPA. The dashed line marks the basalt xenolith (X) boundary.

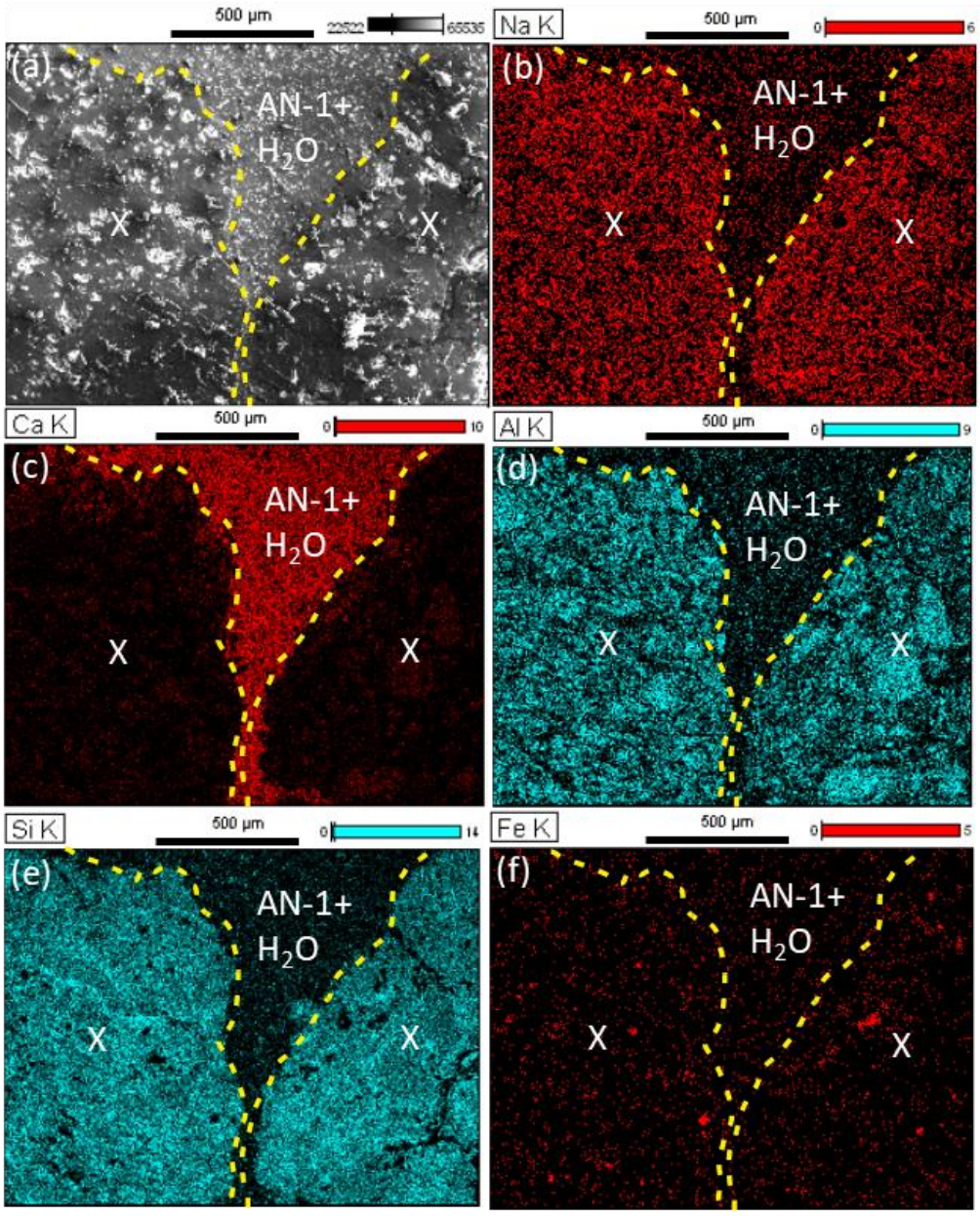

Figure 3.19: Compositional mapping of the KM-11 (at 800 °C and 500 MPa) run product performed using the EMPA. The dashed line marks the andesite xenolith (X) boundary.

KM-10 (Figure 3.18) and KM-11 (Figure 3.19) compositional mapping analysis saw only minor amount of calcium and sodium diffusion along the rims of the basalt and andesite xenoliths. There is minor amounts of titanium and iron segregation in the basalt xenoliths as well as in the matrix as a result of partial melting (Figure 3.18g,h).

3.5 LS-26 + 10wt% H_2O composition

Petrography

The piston cylinder experiments KM-12 (basalt, Figure 3.20) and KM-13 (andesite, Figure 3.21) were conducted at ~500 MPa for 8 hours at 900 °C and 800 °C, respectively with the LS-26 + H_2O mixture. KM-12 run products do not show a great degree of interaction between the basalt xenolith and the LS-26 mixture. Plucking of basalt pieces is observed (Figure 3.20b), along with partial melting inside the basalt xenoliths (Figure 3.20a, c). Diopside and magnetite (Fe-oxide) mineral phases were surrounded by Mg-Fe oxide matrix (Figure 3.20b). Andesite run product resulted in minor diffusion of the xenolith rims (Figure 3.21b), but overall there was lack of interaction between the xenolith and the mixture. SEM analysis of the run products mixtures shows the presence of minerals such as wollastonite, and diopside surrounded by interstitial dolomite-rich carbonate matrix (Figure 3.21c).

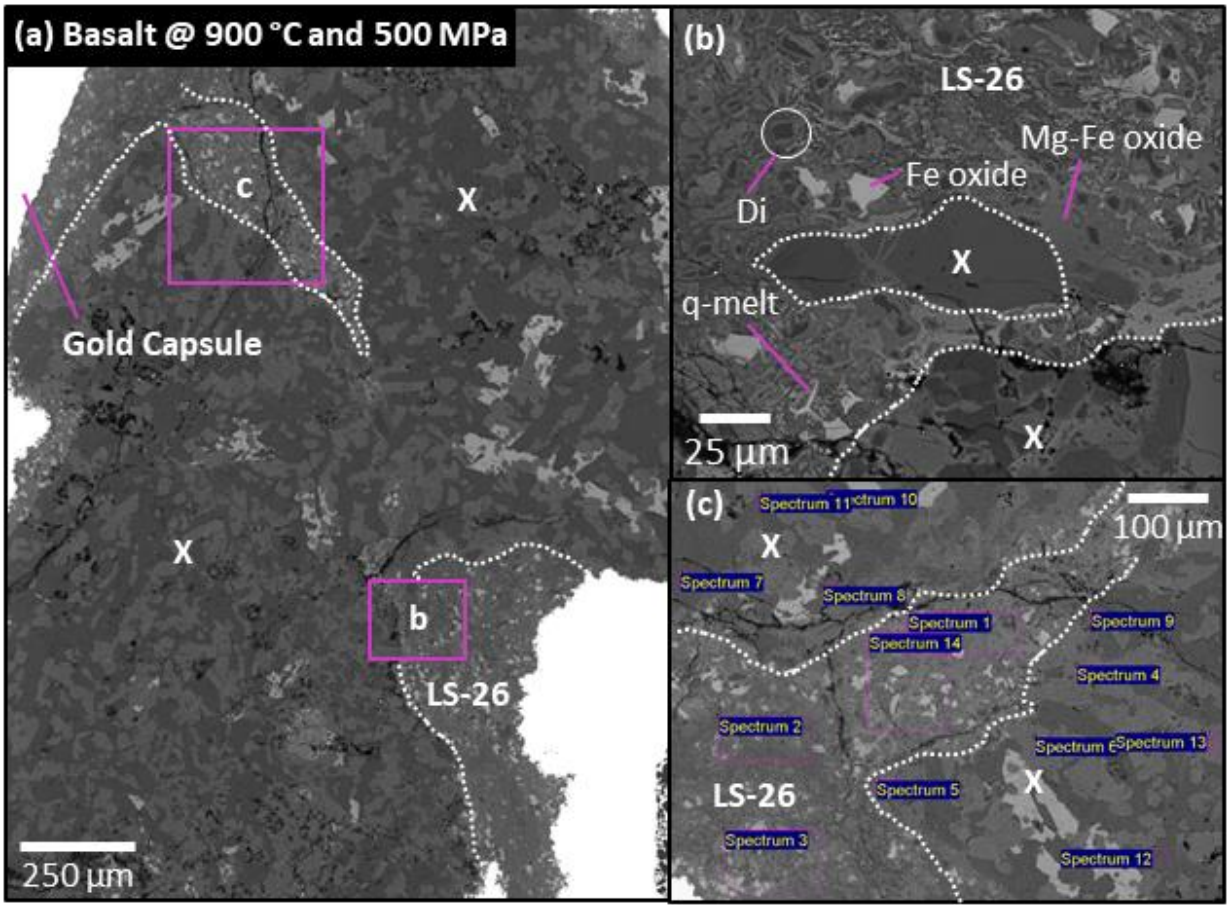

Figure 3.20: (a) Overview of the KM-12 run product with basalt xenoliths (X). Dotted line indicates the xenolith boundary. (b) Shows the interaction of basalt xenolith (X) and the matrix (LS-26). (c) Spectrums 1-3 were used to obtain area compositional analysis using the EDS.

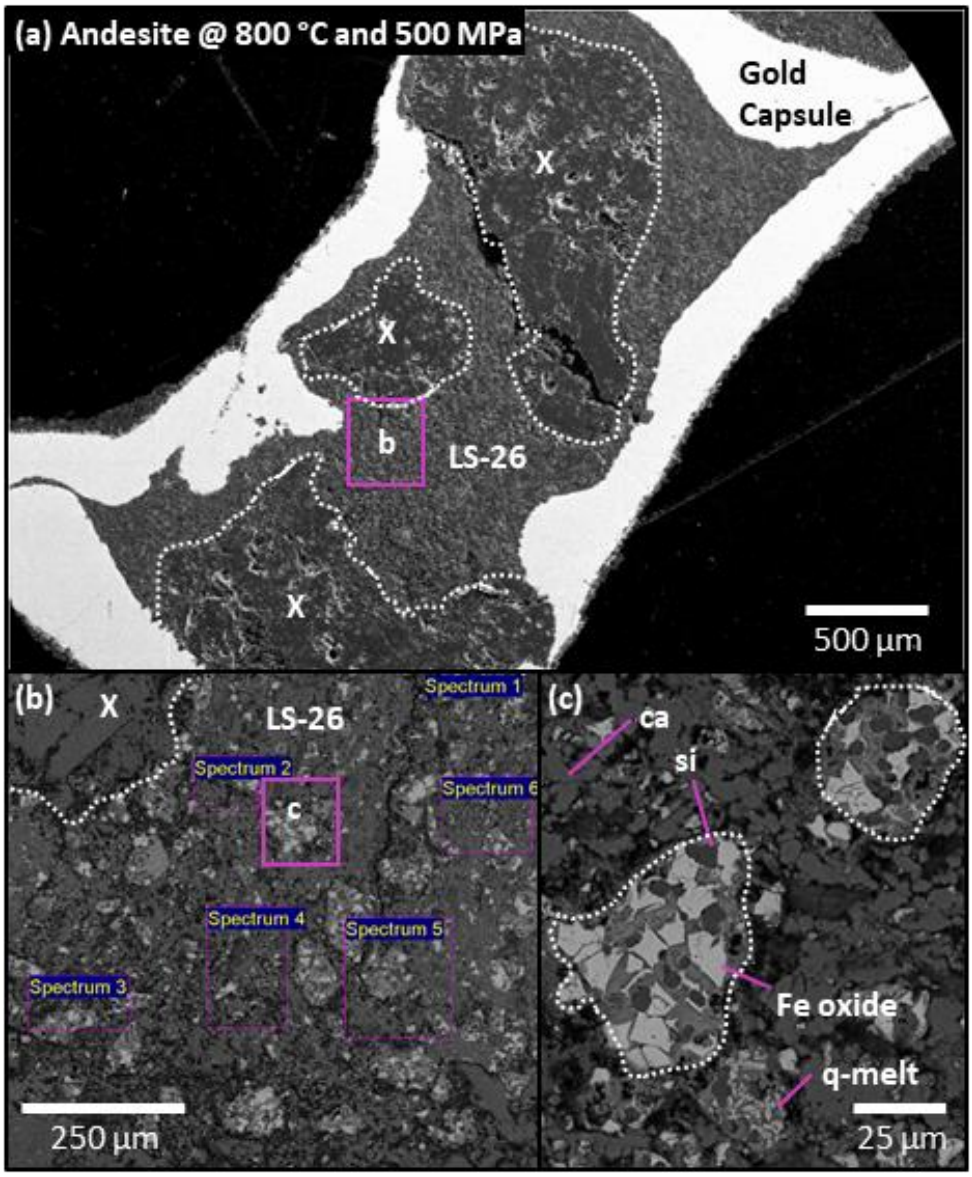

Figure 3.21: (a) Overview of the KM-13 run product with andesite xenoliths (X). Dotted line indicates the xenolith boundary. (b) Shows the interaction of andesite xenolith (X) and the matrix (LS-26). Spectrums 2-6 were used to obtain area compositional analysis using the EDS. (c) *Shows the segregated blobs comprising of quartz (si), Fe-oxides and blobs of quenched melt (q-melt). The blobs are surrounded by impure calcite (ca).*

Table 3.5: Average composition (wt%) of the experimental run products where 'n' indicates the number of area analysis. See Figures 3.5.1c and 3.5.2c for compositional areas. C.I. is the contamination index (See section 4.4).

Oxides (wt%)	LS26	KM-12 (n=3)	KM-13 (n=5)
SiO_2	14.67	29.66	28.12
Al_2O_3	3.06	5.62	5.41
FeO	15.75	22.14	18.66
Na_2O	0.22	1.11	0.52
K_2O	0.72	1.21	0.38
CaO	16.04	19.23	23.05
MgO	19.22	20.96	23.86
CO_2	30.31	-	-
Total	100	100	100
C.I.	0.87	1.56	1.38
ln Si/Al	1.44	1.54	1.52

Table 3.5 shows the average experimental run product composition of KM-12 (basalt) and KM-13 (andesite) compared to the starting LS-26 composition. All major element compositions show an increase in concentrations except for K_2O, which shows minor decrease in concentration. CaO and MgO concentration increases more in andesite run compared to the basalt run, whereas the FeO, K_2O, and Na_2O concentration is higher in basalt run product.

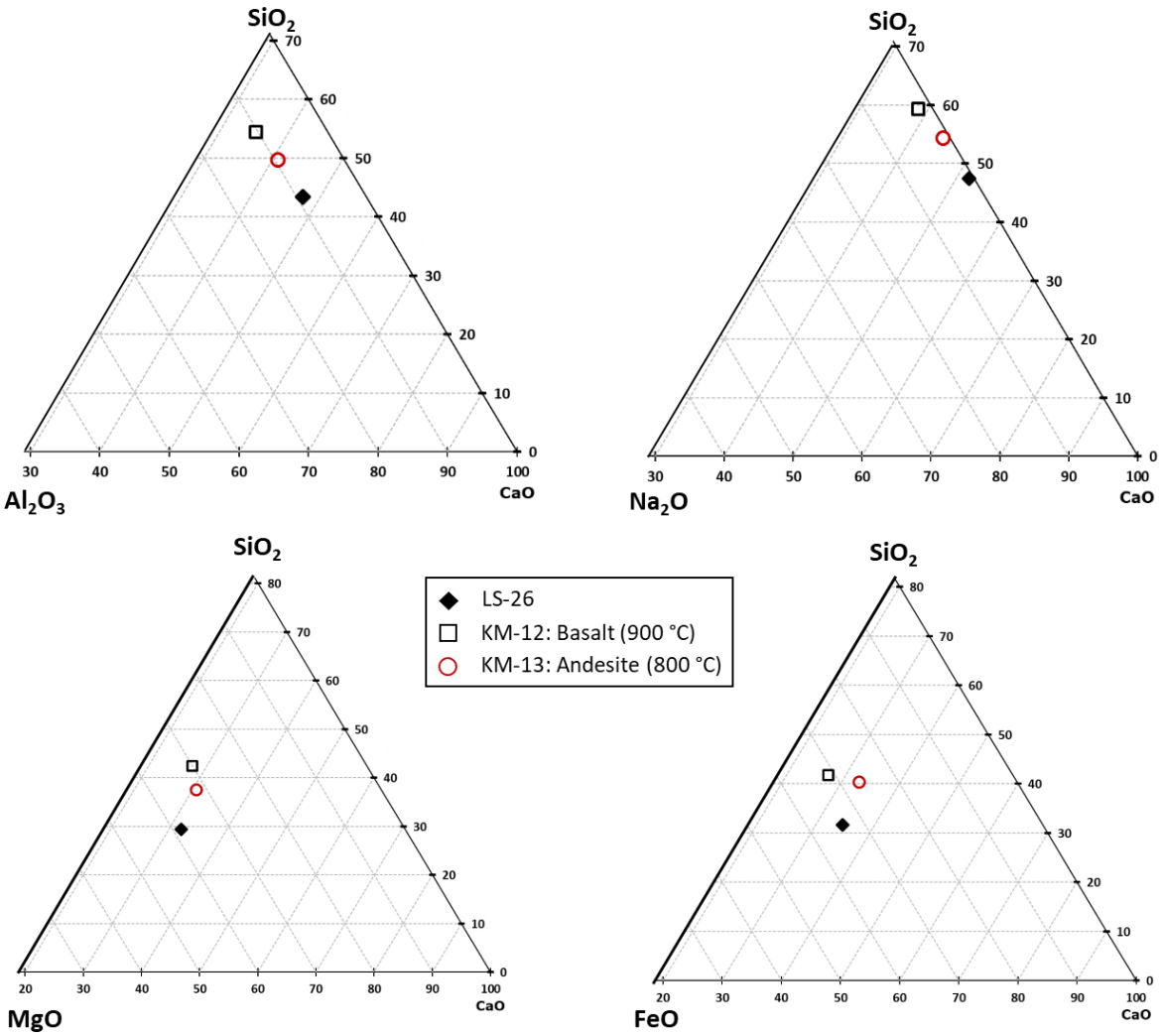

Figure 3.22: Ternary plots of the major elements from the LS-26 + 10wt% H_2O and 500 MPa experimental runs.

The ternary plots (Figure 3.22) displayed a similar trend amongst them with the KM-12 composition appears to be more differentiated than the KM-13 and the starting LS-26 composition. In general, the composition does not vary much and plots in a similar area on the diagrams.

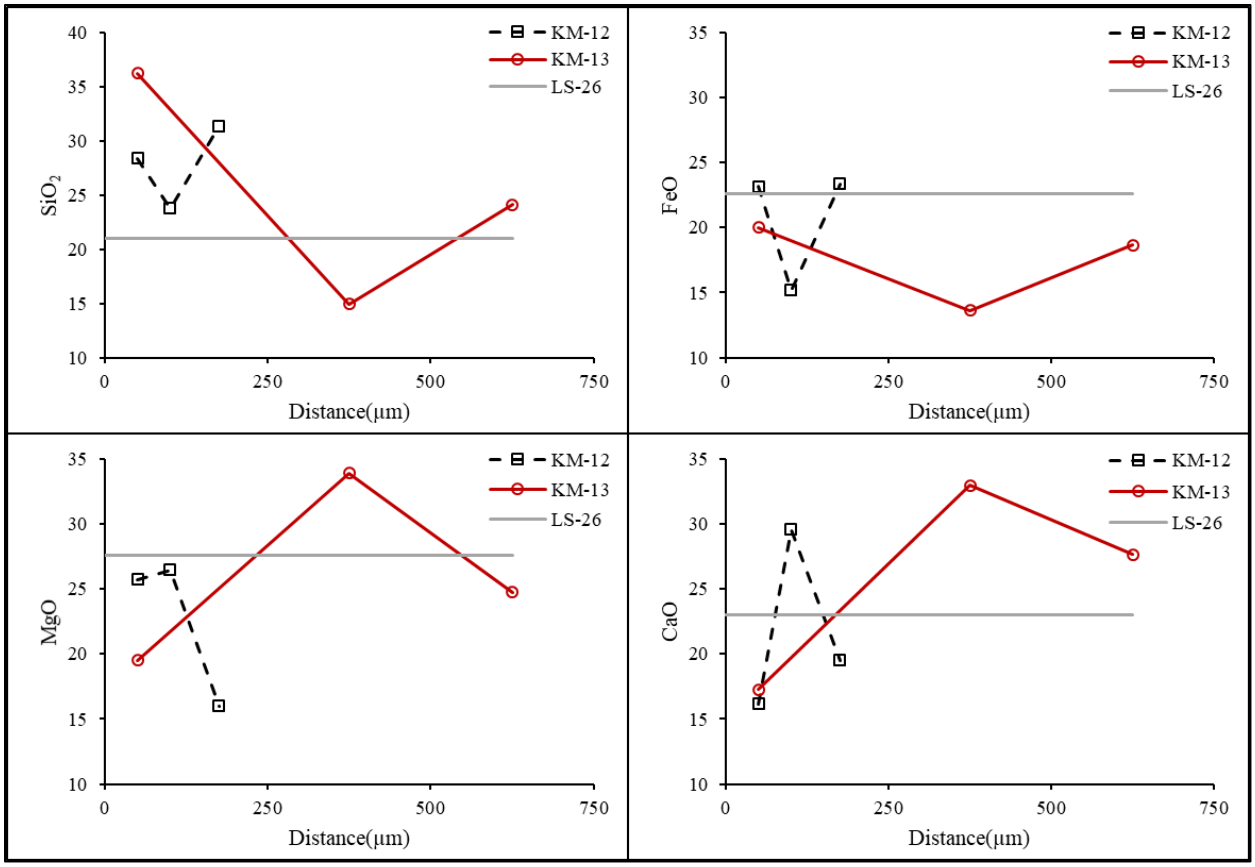

Figure 3.23: Distance profiles of the major elements from the LS-26+10wt% H_2O experimental runs. See table B3 in the appendix B for the compositions, and Figures 3.20c - 3.21b for compositional areas.

Due to small size of the capsules, compositional changes over very small distances were measured. All major elements. Figure 3.23 shows all major element compositions experience a strong increase or decrease in concentration of major elements before averaging out the same compositions as it was close to the xenolith. Overall, both run products KM-12 and KM-13 show similar trends, but in the case of the andesite (KM-13) the compositional changes are more profound due to bigger change in distance.

Compositional Mapping

Compositional mapping analysis shows diffusion of calcium, magnesium towards the rims of the xenoliths in the KM-12 run product (Figure 3.24b,f), and segregation of titanium and iron inside the xenolith due to partial melting (Figure 3.24e,g). Only minor amounts of calcium and aluminum diffusion was noticible around the andesite xenolith

for the KM-13 run product (3.25c,d). All other elements displayed a fairly homogeneous spread.

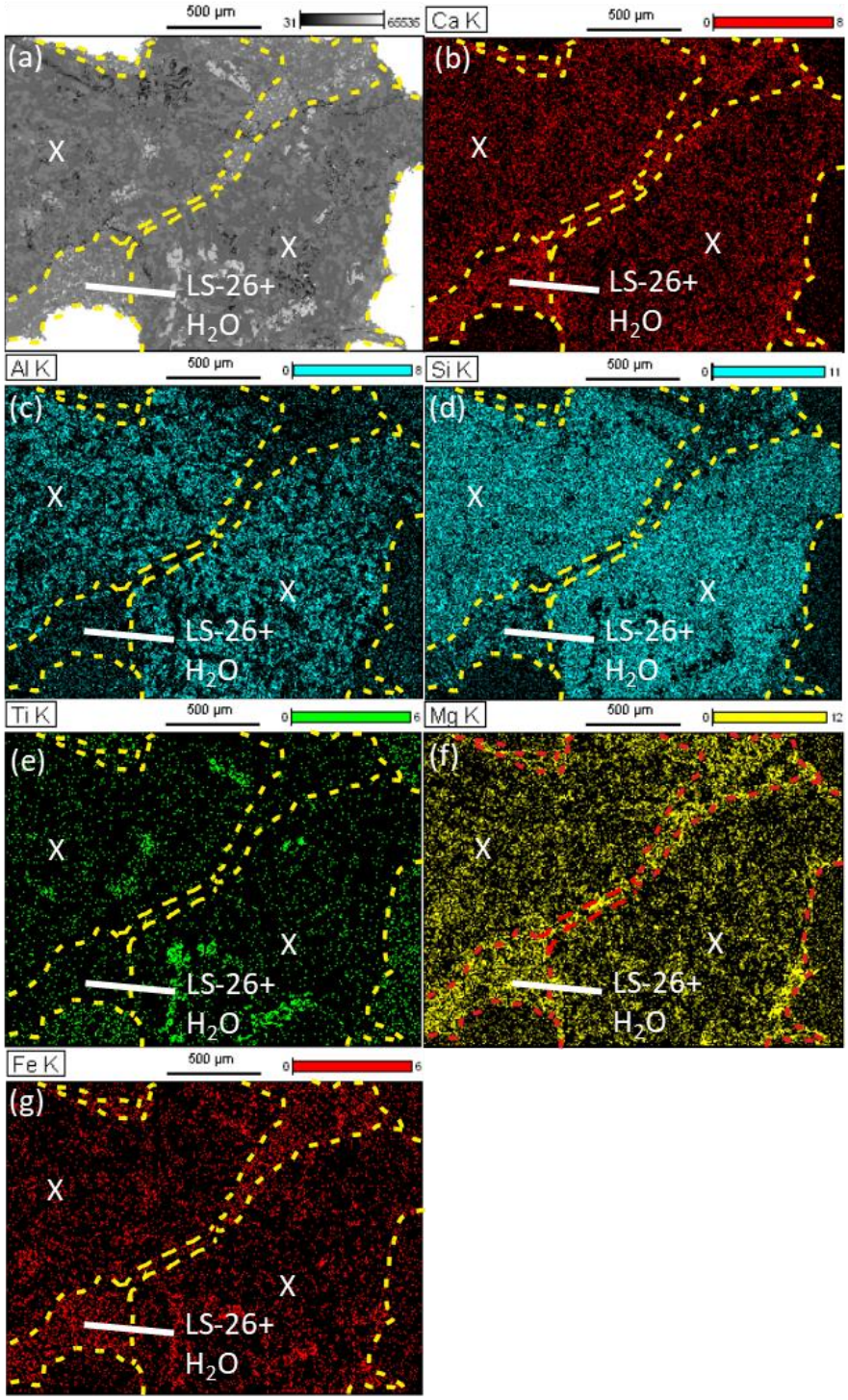

Figure 3.24: Compositional mapping of the KM-12 (at 900 °C) run product performed using the EMPA. The dashed line marks the basalt xenolith (X) boundary.

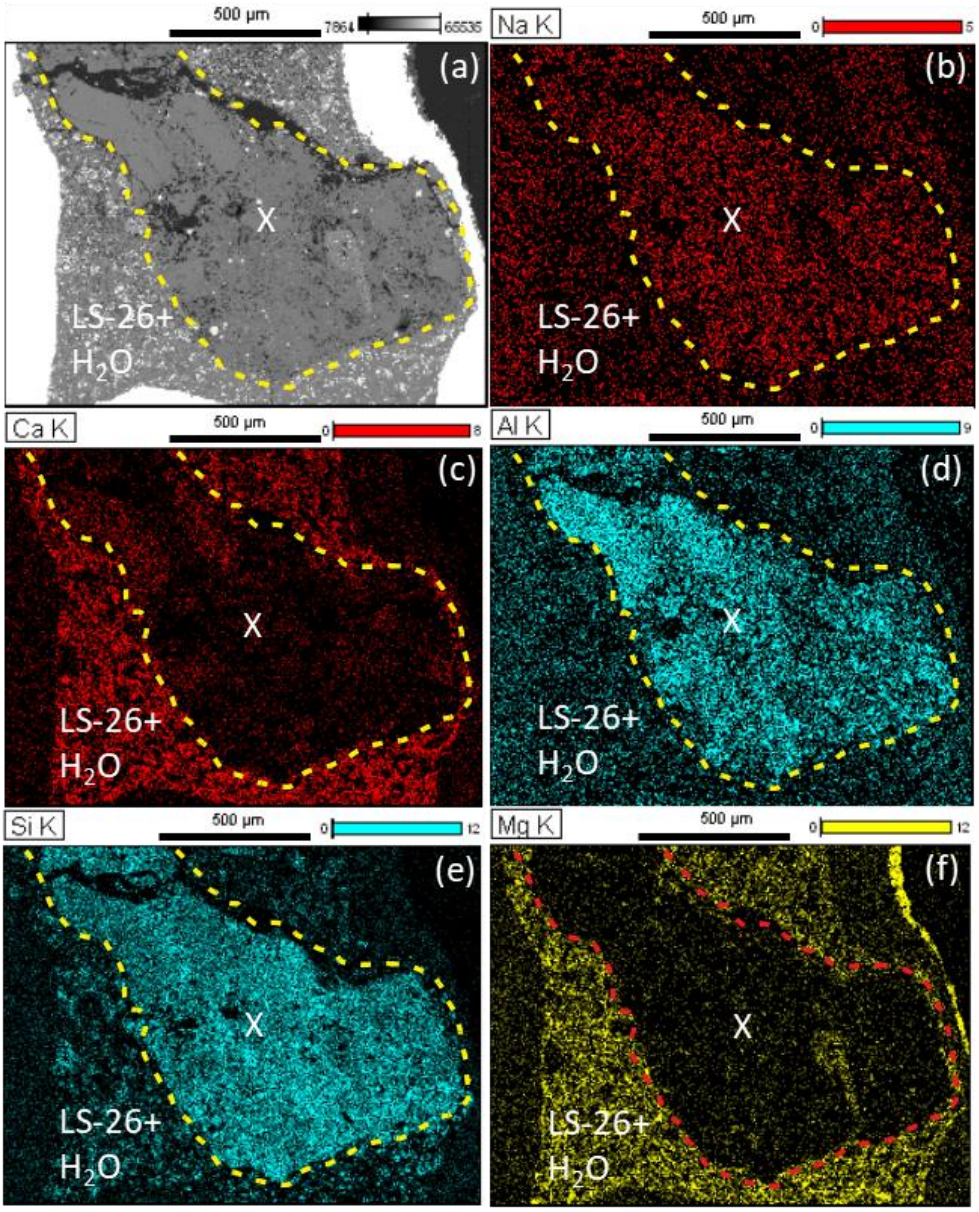

Figure 3.25: Compositional mapping of the KM-13 run product (at 800 °C) performed using the EMPA. The dashed line marks the andesite xenolith (X) boundary.

3.6 Orapa kimberlite

Petrography

Petrographic analysis were done on the natural kimberlite samples from the BK1 kimberlite from Orapa kimberlite cluster, Botswana using the optical petrographic microscope to identify the common mineral phases and textures, and the SEM was used to study the composition of the kimberlite groundmass surrounding the country

rock xenoliths. The results will be compared to that of the experimental run products from this study.

Optical Microscopy

Table 3.6: Optical Microscope analysis of the samples from Orapa kimberlite, Botswana. 'X' indicates the presence of specific mineral. CK and MVK are coherent kimberlites and massive volcaniclastic kimberlites.

Sample	Sample Depth From (m)	Sample Depth To (m)	Perovskite	Carbonate Veins, %	Diopside Rims	Carbonate Segregation	Xenoliths
H002 (CK-A, MVK)							
EGK567	34.53	34.7		65%		X	X
EGK570	42.74	42.96		25%		X	X
EGK572	54.33	54.48		15%		X	X
EGK573	57.34	57.52		30%			
EGK574	61.79	61.98	X				
H003 (CK-A, MVK)							
EGK638	27.12	27.39		55%			
EGK639	32.42	32.64					
EGK640	38.64	38.88		25%		<5%	X
EGK642	55.49	55.76		3%	X	5%	X
EGK643	64.56	64.78			X		X
EGK644	77.93	78.15	X		X		
EGK645	88.23	88.48	X		X		
EGK646	102.35	102.57	X	<1%	X		
EGK647	113.23	113.5		2%	X		
EGK649	135.29	135.5	X		X	X	

The samples from drill-holes H002 and H003 were studied to identify key kimberlite groundmass indicator minerals such as perovskite, diopside, spinel and calcite, as well as examine the presence of carbonate in the matrix. CK-A corresponds to coherent kimberlite which is massive, grey-green in colour with macrocrystic texture and consists of partially assimilated country-rock xenoliths (Table 3.6; Chinn, 2013). Massive volcaniclastic kimberlite (MVK) is a massive, coarse-grained and poorly sorted rock that is matrix supported (Table 3.6; Chinn, 2013). Table 3.6 highlights the minerals that were identified in the thin sections with depth. Both drill-hole samples show presence of carbonate veins at shallower depths along with carbonate segregation (3.26a). Pseudomorphed olivine rims have been surrounded by serpentine or interstitial diopside (Figure 3.26.1a, b). Perovskite and diopside were only present at depths greater than 61.8 m (Figure 3.26b). The basalt xenoliths from both drill holes appears to be highly altered with a presence of reaction rims (Figure 3.26a, c)

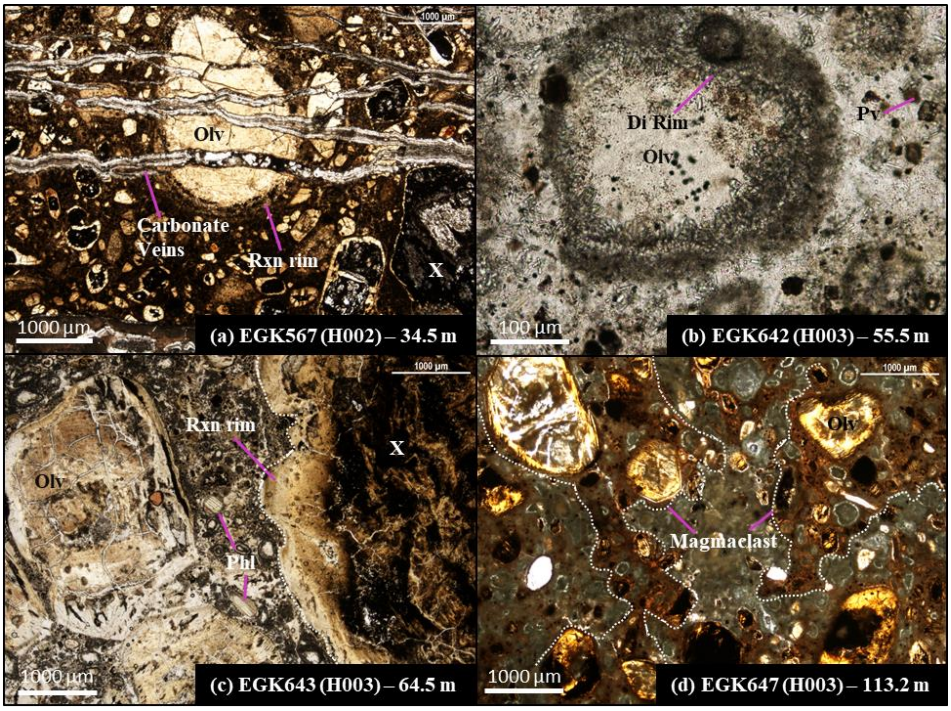

Figure 3.26: Textures and mineral phases observed in the thin section of Orapa kimberlite, Botswana. (a) Carbonate veins overcutting the pseudomorphed olivine (olv) and basalt xenolith (X). (b) Olivine crystal rims being replaced by microlitic diopside (Di Rim). (c) Highly altered basalt xenolith (X) rim being replaced by fine grained serpentine and/or carbonate material. Phologopite (Phl) and pseudomorphed olivine (olv) are present adjacent to the basalt. (d) Typical KPK magmaclasts encompassing the pseudomorphed olivines and other fine-grained minerals.

SEM Mapping

SEM analysis shows presence of thick reaction rims around the highly altered basalt xenolith (3.27a). Further analysis show that the reaction zone consists of rutile, REEs, magnetite, clustered apatites, minor spinel surrounded by serpentine groundmass (Figure 3.27c-d). Clusters of pure quartz surrounded by impure pyroxene matrix were also observed in closed proximity to the xenolith as well (Figure 3.27d).

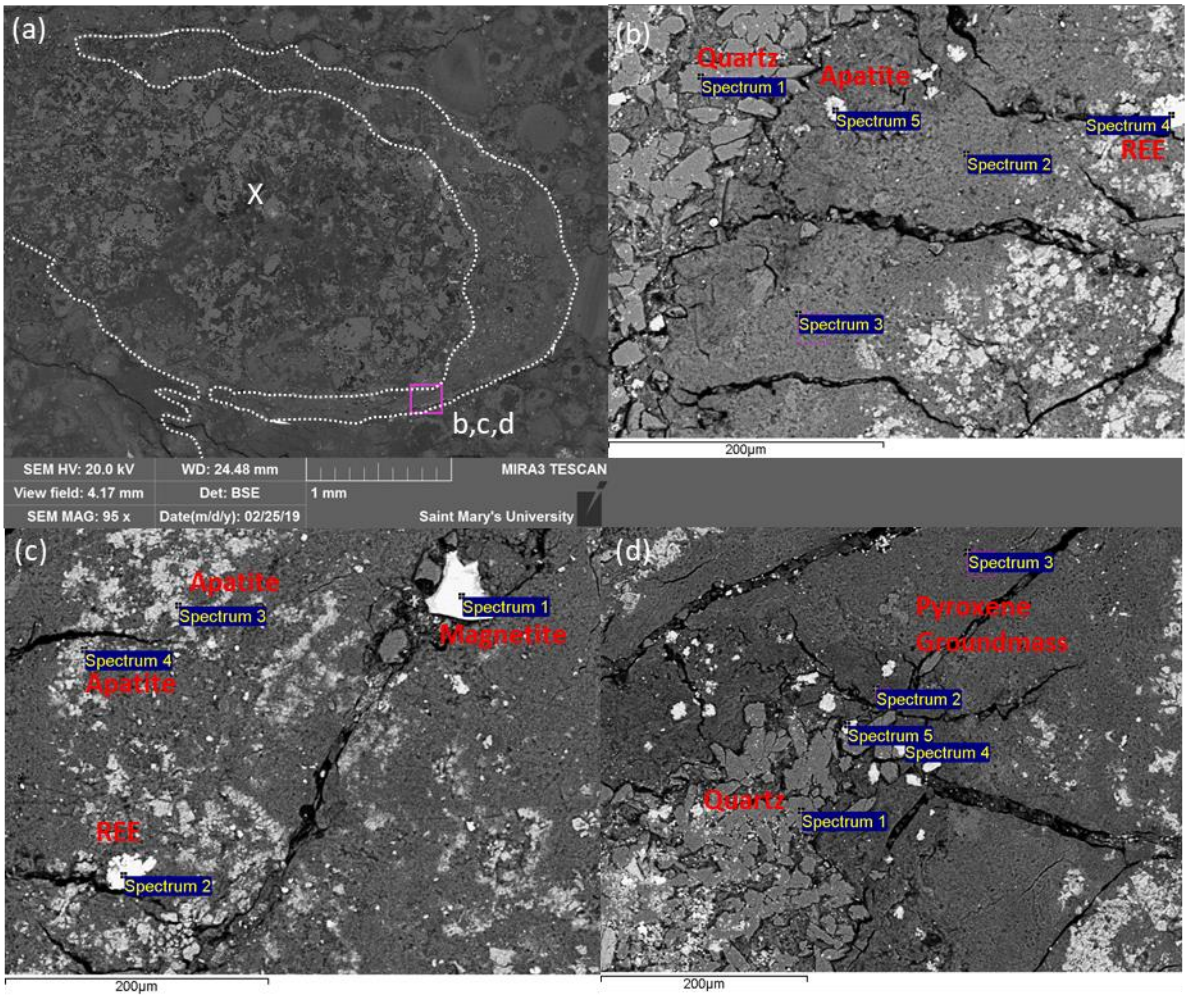

Figure 3.27: SEM642 (H002) analysis using the SEM. (a) Shows the outline of the basalt xenolith (X) adjacent to the reaction zones. The small pink square indicates the area that is further analyzed in more detail.

CHAPTER 4 – Discussion

4.1 The effect of assimilation of crustal rocks on kimberlite magma

Several studies have suggested that reaction between silicate country rocks and carbonate-rich kimberlite magma can notably affect the emplacement behaviour and composition of the kimberlites (Fulop et al., 2018 and Hetman et al., 2004). KPKs host large amounts of crustal xenoliths, which show different degree of assimilation and replacement. According to Caro and Kopylova (2014) assimilation of xenoliths and the kimberlite magma can begin soon after the commencement of crystallization of the groundmass at high temperatures. In the Gahcho Kue kimberlite, contamination of kimberlite magma due to partial or total digestion of country-rock xenoliths lead to crystallization of diopside at higher temperatures whereas pectolite crystallizes from the residual fluid at low temperatures (Caro and Kopylova, 2014). The formation of microlitic diopside or phlogopite can be attributed to changes in crystallization conditions from magmatic to late stage vapour-phase crystallization of residual melt as a result of degassing (Mitchell et al., 2008).

Additionally, a recent detailed petrographic and mineralogical study of the Snap Lake Kimberlite, NWT proposed a skarn-like process (fenitization) process of interaction between fluid and carbonate-rich kimberlite magma and the silicate wall rocks. Petrographic study by Fulop et al. (2018) on the Snap Lake kimberlite dyke shows development of mineral zoning around the altered granite xenoliths, whereas the metavolcanics lack any assimilation around the xenoliths. Mineralogical zoning is dominated by poikilitic phlogophite around the Granitoid xenolith rims and is much more pronounced as compared to minor halos around the metavolcanics (Fulop et al., 2018).

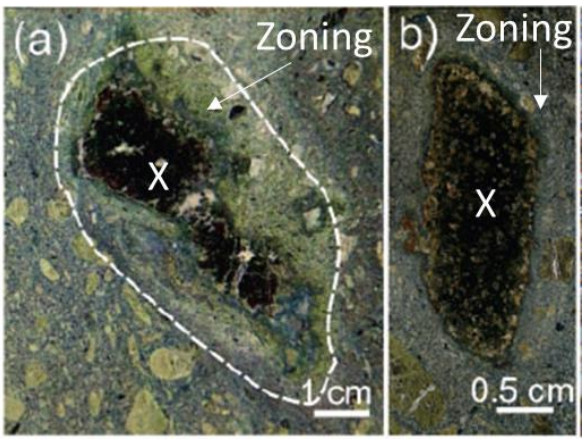

Figure 4.1: Granitoids (X) from the Snap Lake showing the xenolith boundary (dashed line) with zoning halos surrounding the xenoliths. From Fulop et al. (2018).

4.2 Textures and alteration in natural kimberlites

Assimilation of country rock xenoliths can result in contamination of the kimberlite magma. Contamination by Na-rich granite xenoliths at Gahcho Kue resulted in enrichment of Na and Si in the melt (Caro and Kopylova, 2014). The Snap lake kimberlite composition changes gradually with increasing K_2O and decreasing MgO content closer to the xenolith. There is an abrupt jump in CaO concentration along the rim of the veined granitoid xenolith (Fulop et al., 2018). Alteration due to kimberlite magma emplacement resulted in enrichment of MgO, FeO, CaO, K_2O, H_2O and REEs content in the granitoid country rocks of Gahcho Kue (Hetman et al., 2004). The changes in the composition are attributed to the intensity of the granitoid metasomatism as well as the brecciation experienced by the granitoid country rocks (Fulop et al., 2018).

The carbonate groundmass of the Snap Lake kimberlite consists of dolomite away from the granitoid contact (Kopylova et al., 2010), but calcite crystals close to the granitoid contact (Kopylova & Hayman, 2008). Dolomite was found in the in the country rocks surrounding the Gahcho Kue kimberlites and the Orapa kimberlites (See Figure 3.6.1, Hetman et al., 2004). The carbonate rich groundmass is also observed in the Mg-rich LS-26 experimental run products (KM-12, and KM-13). The formation of dolomite groundmass can be attribute to the presence of exsolved CO_2+H_2O near olivine and calcite minerals (Fulop et al., 2018). Although Tracy and Frost (1991, as summarized by

Fulop et al., 2018) suggested the formation of dolomite + silicate (3) at temperature of ~500 °C at 100 MPa, the dolomite for the KM-12 and KM-13 runs formed at 800 °C and ~500 MPa.

$$2Mg_2SiO_4 + CaCO_3 + 2CO_2 + 2H_2O = Mg_3Si_2O_5(OH)_4 + CaMg(CO_3)_2 \quad (3)$$

Olivine Calcite Fluid Serpentine Dolomite

4.3 Textures and alteration of this Study

The results of this experimental study allow us to test the importance of the reactions between the kimberlite melt and the crustal xenoliths, and to examine other factors such as: H_2O, CO_2, temperature, and composition of the xenoliths. Only minor amounts of alteration was observed along the rims of mafic xenoliths. The felsic xenolith alteration was much more evident, and the rims were more diffused. This agrees with the observation made at Snap Lake (Fulop et al., 2018). The xenoliths experienced 2-3 orders magnitude increase in SiO_2, MgO and Al_2O_3 content while the FeO content decreased significantly. This is consistent with the loss of Al_2O_3 and Na_2O, and gain in FeO, CaO, and MgO experienced by natural granitoids of Snap Lake (Fulop et al., 2018).

Increase in CaO and Na_2O content along the rims of the xenolith for the dry AN-1 runs (KM-1- KM-4 and KM-7 – KM-8) is a result of diffusion driven by a large chemical potential gradient between the xenoliths and the carbonate-rich kimberlite mixture. Additionally, Grant (1986) showed that components such as: Na_2O and CaO are considered highly mobile and are more likely to diffuse during metasomatism. This could also explain the abrupt jump in CaO along the rims of natural metasomatized granitic rocks of Snap Lake. The lower content of CaO in the matrix of run products compared to the initial concentrations may be due to relative increase in SiO_2, and partially due to uptake of CaO by newly formed perovskite, as crystals of perovskite were avoided during matrix analysis.

SiO_2 and Al_2O_3 generally show an increase in the matrix after the run. However, their behaviour is controlled by two distinct processes. First, they diffuse from the xenolith into the matrix due to difference in concentration gradient. Secondly, disintegration of minerals such as mica and plagioclase in the xenolith can preferentially

increase the concentration of Al_2O_3. SiO_2 appears to have diffused better and the content increases in run with rhyolite (KM-8), which is due to the combination of diffusional exchange and the disintegration of plagioclase and mica from xenoliths (sources of both SiO_2 and Al_2O_3). Al_2O_3 trends are difficult to interpret. Experiments with molten rhyolite (KM-8) has similar Al_2O_3 concentration as the starting composition, yet there is no evidence of diffusion of Al_2O_3 through the kimberlite matrix. However, all other dry AN-1 run products (KM-3, 4, 7) show an increase in Al_2O_3 concentration, therefore, concentration must have increased by disintegration of xenolith material and mixing into the kimberlite. Disintegration of xenoliths and mixing into the xenoliths is more efficient in the runs with felsic xenoliths. This may explain more profound reaction with granitoids than the mafic country rocks described in Snap Lake.

Meanwhile in the An1+H_2O run products (KM-10 and KM-11), the Al_2O_3 concentration decreases in the kimberlite mixture, which is inconsistent with the results from the dry run and the natural granitoids of snap lake. There is an increase in SiO_2 and CaO due to minor disintegration of plagioclase and diffusional exchange. Experimental runs conducted with LS-26 (KM-12 and KM-13) only show minor increase in SiO_2, which could be attributed to decrease in other elemental concentrations. FeO content shows a decrease in all experimental run products. FeO decrease can partially be explained by diffusion of FeO from the mixtures into the xenoliths. Lack of reaction zones along the rims of xenoliths from this study compared to natural granitoid alteration can be attributed to:

- Lack of assimilation or partial digestion of xenoliths by the kimberlite mixture, and
- Intermediate and mafic country rocks have lower degree of assimilation with kimberlite mixtures compared to felsic rocks.

4.4 Contamination Index

Whole rock composition of kimberlites is affected by a number of contaminants including crustal rocks. The Contamination Index (C.I.) proposed by Clement (1982) evaluates the effects of crustal contamination and/or alteration of kimberlites, and is calculated as:

C.I. = $(SiO_2 + Al_2O_3 + Na_2O)/(MgO + 2K_2O)$ (4)

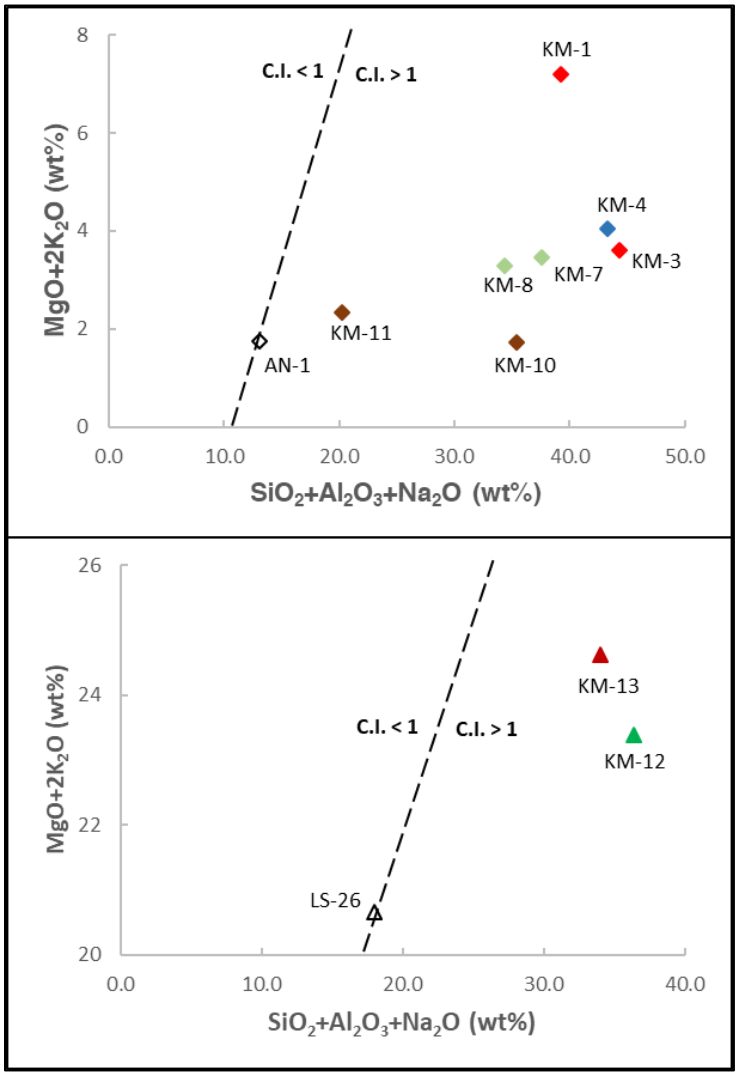

Figure 4.3: Contamination Index for this experimental study based on methods developed by Clement (1982). See tables 3.2, 3.3, and 3.5 for C.I. values. Plot above shows the AN-1 mixture and the plot below shows the LS-25 mixture run product plots, respectively.

Clement (1982) and Mitchell (1986) suggested that the fresh rock have a C.I. < 1. All my run product compositions fall into the contaminated portion of the plot (Figure 4.3). The increase in C.I. in all experimental run products shows that my kimberlite mixtures were indeed contaminated by xenoliths as evident by an increase in SiO_2, Al_2O_3, Na_2O content in the kimberlite melt (table 3.5). Yet, there is a lack of mineralogical zoning around the xenoliths as observed in natural samples. The variation

in the experimental run products are a direct consequence of differentiation processes experienced by the xenoliths and mixtures during each run.

4.5 Effects of CO_2 and H_2O

Presence of bubbles in the matrix of H_2O-bearing runs confirms the presence of H_2O fluid at run conditions (Figure 3.14a and 3.15b). H_2O solubility in silicate melts generally has a much smaller range of compositional dependence than CO_2 (Brooker et al., 2011). Although, water solubility is far less sensitive to compositional changes across common igneous silicate compositions, in some simple analogue systems it appears to increase in response to decreasing silica (Brooker et al., 2011).

Based on the SEM analysis, it appears that the dry runs product (KM-1–KM-4, KM-7, and KM-8) xenoliths reacted better with the AN-1 mixture as compared to the H_2O bearing run xenoliths (KM-9 - KM-13). This aligns with the results of study by Papale et al, (2006), which showed CO_2 solubility can reduce between 30-80% with an addition of ~8.5 wt% water. Experimental work of Moussalam et al. (2016) suggested that CO_2 preferentially exsolves at much shallower depths in the presence of water, therefore, much of the plucking and/or melting occurring along the rims of the xenoliths in this study could be due to CO_2 exsolution. Brooker (2006) suggested that CO_2 solubility will decrease in silicate melts as the Mg/Ca increases. LS-26 mixture Mg/Ca ratio is significantly higher as compared to the AN-1 Mg/Ca ratio which could explain the lack of reaction between the xenolith and the LS-26 mixture.

4.6 Perovskite and change in silica activity

Perovskite is a common groundmass mineral found in kimberlite and carbonatite assemblages. Perovskite was also one of the most common mineral phases that crystallized in the CO_2-rich AN-1 and AN-1+H_2O experiments of this study. In some kimberlites, perovskite is substituted by titanite due to increase in silica activity (5) as a result of metasomatism and/or secondary alteration, which can indicate a higher degree of crustal assimilation (Mitchell and Chakhmouradian, 1998).

$$CaTiO_3 + SiO_2 \rightarrow CaTiSiO_5 \qquad (5)$$

Perovskite liquid Titanite

The SiO_2 activity of the normal evolution of kimberlite magma is within perovskite stability field (Figure 4.3; Luth, 2009). In addition, Mitchell and Chakhmouradian (1998) suggested that perovskite becomes unstable in the presence of carbonate fluids, where the substitution happens by the following reactions (6) and further crystallization of anatase with titanite due to increase in silica activity (7):

$$\underset{\text{Perovskite}}{2CaTiO_3} + CO_2 + H_2O \rightarrow \underset{\text{Kassite}}{CaTi_2O_4(OH)_2} + \underset{\text{Calcite}}{CaCO_3} \quad (6)$$

$$\underset{\text{Kassite}}{CaTi_2O_4(OH)_2} + \underset{\text{liquid}}{SiO_2} \rightarrow \underset{\text{Anatase}}{2TiO_2} + \underset{\text{Titanite}}{CaTiSiO_5} + H_2O \quad (7)$$

However, my data does not confirm this. My compositions are very carbonate rich and had CO_2 fluid present, and yet the perovskites that formed appears to be perfectly stable. Mitchell and Chakhmouradian (1998) suggested a range of 500-600 °C in order for the perovskite replacement to occur. My data demonstrate that perovskite is stable phase at 800 °C – 1100 °C in a carbonate-rich composition. Additionally, none of my experiments produced titanite even close to the proximity of the xenoliths as well as in the experiments with molten rhyolite. The reaction between carbonate-rich kimberlite mixture and silicate xenoliths of my experiments was not sufficient to stabilize titanite, instead forming perovskite.

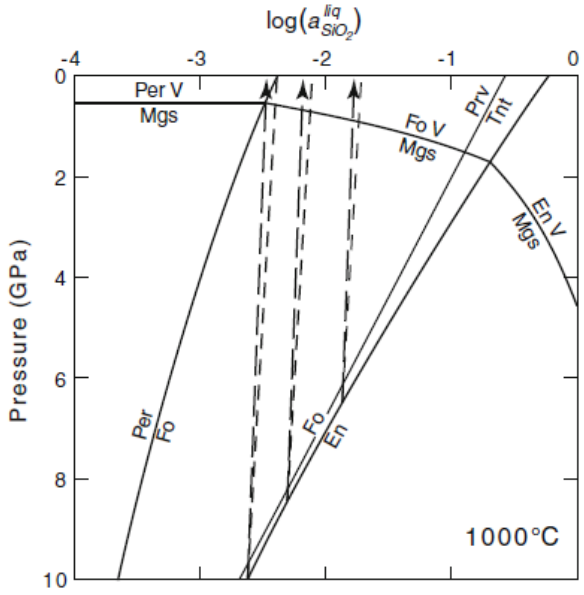

Figure 4.3: Isothermal P-log(a_{SiO2}^{liq}) diagram with Perovskite-Titanite (Prv-Ttn) curve showing the stability field of the minerals at 1000 °C. From Luth (2009).

4.7 KPK Features

KPKs are distinct from other kimberlites due to their distinct physical and mineralogical properties such as: presence of up to 70 vol% crustal xenoliths, and formation of reaction and diopside rims around contaminated xenoliths and pseudomorphed olivines. In my study, my experiments failed to form reaction or diopside rims. More over, both the low and high Mg content mixture compositions (AN-1 and LS-26, respectively) failed to fully react with the crustal felsic and mafic xenoliths. Although, the duration of KPK magma eruption is unknown, we used range of temepratures (800 °C – 1100 °C) and the durations (1 hour to 8 hours) to try to re-produce the natural KPK features. Based on my experimental results, the sub-fluidization model cannot be the only process that leads to the formation of distinct KPK textures around the world.

CHAPTER 5 – CONCLUSION

5.1 Summary

The study experimented with four different carbonate-rich kimberlite mixtures, and mafic and felsic xenoliths in an attempt to reproduce the textures observed in natural kimberlites. We discovered that the effects of CO_2 were much more profound in the runs at 0.1 MPa as compared to water bearing runs which saw minimal assimilation of country rock xenoliths with the kimberlite mixtures. The study also showed that the felsic rock xenoliths were able to assimilate better with the kimberlite mixtures as compared to intermediate and mafic rocks. This is in line with the reactions textures studied at the Snap Lake kimberlite where the granitoids experienced greater degree of assimilation due to fentinization as compared to the metavolcanics. Mobile components such as calcium and sodium were able to diffuse towards the boundary between xenoliths and the mixture due to compositional gradient as a result of metasomatic activity. Similar positive spike in CaO concentration along the rims of the granitoids of Snap Lake kimberlite. Gahcho Kue, Snap Lake, and BK1 kimberlites showed formation of diopside and phlogopite mineral phases, which were not produced in my study because of the composition and the temperatures used in the study. Formation of perovskite minerals phase instead of titanite was a result of the expansion of the stability field of perovskite at shallower levels.

Results of my study suggests that CO_2 degassing plays a crucial role during the ascent of the kimberlite magma especially at depths similar to KPKs emplacement and will result in country rock brecciation, and magma fragmentation and freezing. The addition of H_2O reduces the CO_2 solubility in the mixtures, thereby reducing the effectiveness of kimberlite magma to breach the surface.

5.2 Future work

Experiments with the LS-26 mixture at 0.1 atm are required to further understand the behaviour of high magnesium compositions and its interaction with the mafic and felsic xenoliths. Mineral phases such as quartz and other Mg- and/or Fe-oxides surrounded by carbonate that were observed in the KM-12 and KM-13 runs are similar

to minerals that were observed in Orapa thin sections. Additionally, it would be interesting the see if we are able to reproduce the same mineral assemblage in the run at 0.1 atm with LS-26 mixture. CO_2 measurements in the run product compositions can help better understand the degree of CO_2 degassing experienced by rocks at shallower depths.

CHAPTER 6 – References

Brooker, R. A. (2006). The role of experiments and theory in understanding volatile control on the kimbertlie eruption mechanism. The Kimberlite Emplacement Workshop, 8th International Kimberlite Conference, Saskatoon, September 2006.

Brooker, R. A., Sparks, R. S. J., Kavanagh, J. L., & Field, M., 2011. The volatile content of hypabyssal kimberlite magmas: some constraints from experiments on natural rock compositions. Bulletin of Volcanology, 73, 959-981.

Canil, D., & Fedortchouk, Y., 1999. Garnet dissolution and the emplacement of kimberlites. Earth and Planetary Science Letters, 167, 227-237.

Caro, G., Kopylova, M. G., & Creaser, R. A., 2004. The hypabyssal 5034 kimberlite of the Gahcho Kue cluster, southeastern Slave craton, Northwest Territories, Canada: a granite-contaminated Group-I kimberlite. The Canadian Mineralogist, 42, 183-207.

Chinn, I., 2013. BK1 Kimberlite notes for Yana.

Clement, C.R., 1982. A comparative geological study of some major kimberlite pipes in the Northern Cape and Orange Free State. Ph.D. thesis University of Cape Town.

Das, J. N., Korakoppa, M. M., Shivanna, S., Srivastava, J. K., & Gera, N. L., 2013. Tuffisitic kimberlite from Eastern Dharwar craton, Undraldoddi area, Raichur district, Karnataka, India. In Proceedings of 10th International Kimberlite Conference. pp. 109-128. Springer, New Delhi.

Grant, J. A., 1986. The isocon diagram; a simple solution to Gresens' equation for metasomatic alteration. *Economic geology*, *81*, 1976-1982.

Field, M. & Scott Smith, B. H., 1998. Textural and genetic classification schemes for kimberlites: a new perspective. In International Kimberlite Conference: Extended Abstracts, Vol. 7, pp. 214-216.

Fulop, A., Kopylova, M., Kurszlaukis, S., Hilchie, L., Ellemers, P., & Squibb, C., 2018. Petrography of Snap Lake kimberlite dyke (Northwest Territories, Canada) and its interaction with country rock granitoids. Journal of Petrology, 59, 2493-2518.

Hetman, C. M., Smith, B. S., Paul, J. L., & Winter, F., 2004. Geology of the Gahcho Kué kimberlite pipes, NWT, Canada: root to diatreme magmatic transition zones. Lithos, 76, pp. 51-74.

Hetman, C. M. 2008. Tuffisitic kimberlite (TK): A Canadian perspective on a distinctive textural variety of kimberlite. Journal of Volcanology and Geothermal Research, 174, 57-67.

Kjarsgaard, B. A., Pearson, et al., 2009). Geochemistry of hypabyssal kimberlites from Lac de Gras, Canada: comparisons to a global database and applications to the parent magma problem. Lithos, 112, 236-248.

Lorenz, V., 1975. Formation of phreatomagmatic maar-diatreme volcanoes and its relevance to kimberlite diatremes. Physics and Chemistry of the Earth. 9, pp. 17-27.

Mitchell, R. H., 1986. Kimberlites: mineralogy, geochemistry, and petrology. Springer Science & Business Media.

Luth, R. W., 2009. The activity of silica in kimberlites, revisited. Contributions to Mineralogy and Petrology, 158, 283-294.

Mitchell, R. H., & Chakhmouradian, A. R., 1998. Instability of perovskite in a CO_2-rich environment; examples from carbonatite and kimberlite. The Canadian Mineralogist, 36, 939-951.

Mitchell, R. H., & Kjarsgaard, B. A., 2008. Experimental studies of the system $Na_2Ca(CO_3)_2$–NaCl–KCl at 0.1 GPa: implications for the differentiation and low-temperature crystallization of natrocarbonatite. The Canadian Mineralogist, 46, 971-980.

Mitchell, R. H., Skinner, E. M. W., & Smith, B. H. S., 2009. Tuffisitic kimberlites from the Wesselton Mine, South Africa: Mineralogical characteristics relevant to their formation. Lithos, 112, pp. 452-464.

Moussallam, Y., Morizet, Y., & Gaillard, F., 2016. H2O–CO2 solubility in low SiO2-melts and the unique mode of kimberlite degassing and emplacement. Earth and Planetary Science Letters, 447, 151-160.

Papale, P., Moretti, R., & Barbato, D., 2006. The compositional dependence of the saturation surface of H2O+ CO2 fluids in silicate melts. *Chemical Geology*, *229*, 78-95.

Scott Smith, B. H., 2008. Canadian kimberlites: geological characteristics relevant to emplacement. Journal of Volcanology and Geothermal Research, 174, pp. 9-19.

Scott Smith, B. H., & Smith, S. C., 2009. The economic implications of kimberlite emplacement. Lithos, 112, pp. 10-22.

Scott Smith, B. H., Nowicki, T. E., et. al., 2018. A glossary of kimberlite and related terms – Part 1 Glossary. Scott-Smith Petrology Inc., Vancouver, Canada.

Skinner, E. M. W., & Marsh, J. S., 2004. Distinct kimberlite pipe classes with contrasting eruption processes. Lithos, 76, pp. 183-200.

Skinner, E. M. W., 2008. The emplacement of class 1 kimberlites. Journal of Volcanology and Geothermal Research, 174, pp. 40-48.

Sparks, R. S. J., Baker, L., et. al., 2006. Dynamical constraints on kimberlite volcanism. Journal of Volcanology and Geothermal Research, 155, pp. 18-48.

Walters, A. L., Phillips, J. C., Brown, R. J., et. al., 2006. The role of fluidisation in the formation of volcaniclastic kimberlite: grain size observations and experimental investigation. Journal of volcanology and geothermal research, 155, pp. 119-137.

Winter, J. D., 2010. Principles of igneous and metamorphic petrology. Pearson Education.

Wooley, A.R., Bergman, S., Edgar, A.D., Le Bas, M.J., Mitchell, R.H., Rock, N.M.S., Scott Smith, B.H., 1995. Classification of lamprophyres, lamproites, kimberlites, and the kalsilite-, melilite-, and leucite-bearing rocks. Canadian Mineralogist. 32, pp. 175-186.

APPENDIX A

See attached excel file "Appendix A" for area compositional analysis of all experimental run products.

APPENDIX B

Table B1: AN-1 experimental run product compositions used for distance profiles.

	KM-3	KM-3	KM-3	KM-4	KM-4	KM-4	KM-7	KM-7	KM-7	KM-8	KM-8	KM-8	KM-8
Distance (μm)	100	450	850	150	600	850	100	650	800	300	500	825	1300
SiO2	20.77	25.37	22.39	16.93	15.10	15.62	23.49	19.90	19.80	23.10	21.94	19.10	18.57
TiO2	7.27	1.41	1.58	0.96	6.04	3.89	1.56	4.26	2.07	0.90	6.82	3.08	1.27
Al2O3	21.08	17.46	19.61	27.27	22.92	23.18	11.20	15.30	20.45	8.73	9.78	9.09	8.56
FeO	1.82	2.04	2.24	1.64	1.35	1.14	2.07	1.38	1.82	1.54	1.82	1.90	1.83
Na2O	1.11	4.10	1.33	2.40	1.87	2.28	1.98	2.42	0.66	0.93	0.77	2.51	1.41
K2O	0.22	0.94	0.31	0.08	-	-	0.17	0.49	0.15	0.18	0.00	0.47	0.12
CaO	45.03	45.92	50.12	48.72	50.92	52.30	56.07	53.81	52.42	61.23	55.14	60.60	65.91
MgO	2.70	2.76	2.42	2.00	1.80	1.55	3.46	2.45	3.12	3.39	3.72	3.26	2.35
CO2	-	-	-	-	-	-	-	-	-	-	-	-	-
Total	100	100	100	100	100	99.96	100	100	100	100	100	100	100

Table B2: AN-1+H_2O experimental run product compositions used for distance profiles.

	KM-10	**KM-10**	**KM-10**	**KM-11**	**KM-11**	**KM-11**	**KM-11**
Distance(μm)	150	400	700	50	300	450	700
SiO2	13.94	17.00	15.77	16.91	14.82	14.92	16.87
TiO2	10.15	1.70	5.21	2.91	4.6	2.18	1.88
Al2O3	2.97	3.51	5.42	2.01	3.47	3.47	4.11
FeO	1.18	1.00	1.19	1.2	1.16	1.17	1.53
Na2O	2.79	3.36	3.48	0.63	1.28	1.14	1.52
K2O	0.00	0.00	0.00	0.08	0.25	0.25	0.36
CaO	67.62	71.19	66.97	74.58	72.38	74.96	71.96
MgO	1.60	2.01	1.84	1.68	2.04	1.92	1.77
Total	100	100	100	100	100	100	100

Table B3: LS-26+H_2O experimental run product compositions used for distance profiles.

	KM-12	KM-12	KM-12	KM-13	KM-13	KM-13
Distance (μm)	50	100	175	50	375	625
SiO2	28.38	23.75	31.36	36.23	14.94	24.12
Al2O3	5.23	3.68	6.7	5.73	4.13	4.4
FeO	23.16	15.18	23.36	20.01	13.62	18.66
Na2O	0.56	0.46	1.26	0.67	0.34	0.26
K2O	0.58	0.78	1.84	0.6	0.11	0.16
CaO	16.16	29.56	19.51	17.25	32.96	27.63
MgO	25.74	26.48	16.01	19.51	33.91	24.76
Total	100	100	100	100	100	100